HHS Public Access

Author manuscript

Cell. Author manuscript; available in PMC 2024 August 03.

Published in final edited form as:

Cell. 2023 August 03; 186(16): 3350–3367.e19. doi:10.1016/j.cell.2023.06.004.

Development of an α-synuclein positron emission tomography tracer for imaging synucleinopathies

Jie Xiang[1,2,17], **Youqi Tao**[3,4,17], **Yiyuan Xia**[1,5,6,17], **Shilin Luo**[1,7], **Qinyue Zhao**[3,4], **Bowei Li**[8], **Xiaoqian Zhang**[9], **Yunpeng Sun**[10], **Wencheng Xia**[10], **Mingming Zhang**[10], **Seong Su Kang**[1], **Eun-Hee Ahn**[1], **Xia Liu**[1], **Fang Xie**[11], **Yihui Guan**[11], **Jenny J. Yang**[12], **Lihong Bu**[13], **Shengxi Wu**[2], **Xiaochuan Wang**[5], **Xuebing Cao**[9], **Cong Liu**[10,14], **Zhentao Zhang**[15,*], **Dan Li**[3,4,*], **Keqiang Ye**[1,16,18,*]

[1]Department of Pathology and Laboratory Medicine, Emory University School of Medicine, Atlanta, GA 30322, USA

[2]Department of Neurobiology, Fourth Military Medical University, Xi'an, China

[3]Bio-X Institutes, Key Laboratory for the Genetics of Developmental and Neuropsychiatric Disorders, Ministry of Education, Shanghai Jiao Tong University, Shanghai, China

[4]Zhangjiang Institute for Advanced Study, Shanghai Jiao Tong University, Shanghai 200240, China

[5]Department of Pathophysiology, Tongji Medical College, Huazhong University of Science and Technology, Wuhan, China

[6]Institute of Biomedical Sciences, School of Medicine, JiangHan University, #8, Sanjiaohu Rd., Wuhan 430056, China

[7]Department of Pharmacy, the Second Xiangya Hospital, Central South University, Changsha, China

[8]Shenzhen Institute of Advanced Technology, University of Chinese Academy of Science, Shenzhen, Guangdong 518055, China

[9]Department of Neurology, Union Hospital, Tongji Medical College, Huazhong University of Science & Technology, Wuhan 430022, China

[*]Correspondence: zhentaozhang@whu.edu.cn (Z.Z.), lidan2017@sjtu.edu.cn (D.L.), kq.ye@siat.ac.cn (K.Y.).

AUTHOR CONTRIBUTIONS

K.Y., D.L., and Z.Z. conceived the project, designed the experiments, analyzed the data, and wrote the manuscript. J.X., Y.X., and S.L. performed most of the experiments. X.Z., S.S.K., E.-H.A., and X.L. prepared primary neurons and assessed them with animal experiments. L.B., F.X., and Y.G. conducted the microPET imaging and radio-labeling ^{18}F-compound 8b and F0502B. C.L., Y.T., and Q.Z. prepared cryo-EM samples. M.Z., Y.T., W.X., and Q.Z. performed cryo-EM data collection. Y.T. and Q.Z. performed cryo-EM data processing, helical reconstruction, and atomic model building. Y.S. assisted in cryo-EM data processing. J.J.Y., C.L., S.W., X.W., and X.C. assisted with data analysis and interpretation and critically read the manuscript. All of the authors were involved in analyzing the data and contributed to manuscript discussion and editing.

SUPPLEMENTAL INFORMATION

Supplemental information can be found online at https://doi.org/10.1016/j.cell.2023.06.004.

DECLARATION OF INTERESTS

K.Y. is a co-founder of Shanghai Braegen Pharmaceuticals, Inc. that licensed the PET tracer patent from Emory University. No data are sponsored by the company.

[10]Interdisciplinary Research Center on Biology and Chemistry, Shanghai Institute of Organic Chemistry, Chinese Academy of Sciences, Shanghai 201210, China

[11]Department of Nuclear Medicine & PET Center, Huashan Hospital, Fudan University, Shanghai, China

[12]Department of Chemistry, Georgia State University, Atlanta, GA 30303, USA

[13]PET-CT/MRI Center, Renmin Hospital of Wuhan University, Wuhan 430060, China

[14]State Key Laboratory of Chemical Biology, Shanghai Institute of Organic Chemistry, Chinese Academy of Sciences, Shanghai 200032, China

[15]Department of Neurology, Renmin Hospital of Wuhan University, Wuhan 430060, China

[16]Faculty of Life and Health Sciences, Shenzhen Institute of Advanced Technology, Chinese Academy of Sciences, Shenzhen, Guangdong 518055, China

[17]These authors contributed equally

[18]Lead contact

SUMMARY

Synucleinopathies are characterized by the accumulation of α-synuclein (α-Syn) aggregates in the brain. Positron emission tomography (PET) imaging of synucleinopathies requires radiopharmaceuticals that selectively bind α-Syn deposits. We report the identification of a brain permeable and rapid washout PET tracer [^{18}F]-F0502B, which shows high binding affinity for α-Syn, but not for Aβ or Tau fibrils, and preferential binding to α-Syn aggregates in the brain sections. Employing several cycles of counter screenings with *in vitro* fibrils, intraneuronal aggregates, and neurodegenerative disease brain sections from several mice models and human subjects, [^{18}F]-F0502B images α-Syn deposits in the brains of mouse and non-human primate PD models. We further determined the atomic structure of the α-Syn fibril-F0502B complex by cryo-EM and revealed parallel diagonal stacking of F0502B on the fibril surface through an intense noncovalent bonding network via inter-ligand interactions. Therefore, [^{18}F]-F0502B is a promising lead compound for imaging aggregated α-Syn in synucleinopathies.

Graphical Abstract

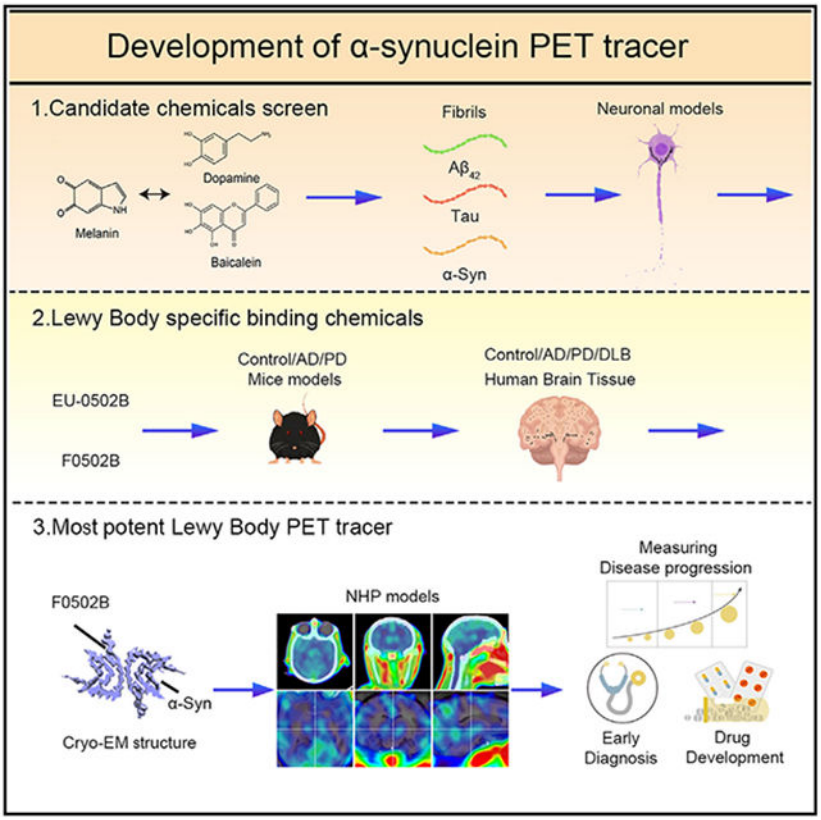

In brief

Development and structural characterization of a specific, high-affinity α-synuclein PET tracer for synucleinopathy imaging.

INTRODUCTION

Neurodegenerative disorders displaying aggregated α-synuclein (α-Syn) deposits in the brain are called synucleinopathies and include clinical entities such as Parkinson disease (PD), PD dementia (PDD), dementia with Lewy bodies (DLBs), and multiple system atrophy (MSA). In contrast to the intraneuronal insoluble α-Syn inclusions in PD, PDD, and DLB, α-Syn aggregates in MSA occur predominantly in the form of glial cytoplasmic inclusions.[1] α-Syn normally adopts an intrinsically disordered conformation.[2] Under diseased circumstances, it undergoes a profound conformational transition to a β sheet-rich structure that polymerizes into pathological amyloid fibrils. The misfolded protein may act as a template to promote the misfolding of host α-Syn. Thus, α-Syn can act as a prion-like protein adopting a self-propagating conformation.[3-5] Emerging evidence suggests that α-Syn pathology propagates across interconnected networks throughout the nervous system in a prion-like manner. Pathologic α-Syn seeds aggregation of native α-Syn, resulting in the formation of insoluble inclusions. These seeds can propagate both within the neurons and to interconnected neurons, resulting in the spread of pathology throughout the brain.[6,7] Noticeably, the co-occurrence of different disease protein aggregates in the same patient is

frequently observed. More than 50% of neuropathologically confirmed Alzheimer disease (AD) cases show α-Syn aggregates, whereas co-morbid AD pathologies, including compact amyloid-beta (Aβ) plaques and neurofibrillary tangles (NFTs), are commonly found in PD, PDD, and DLB brains.[8] Positron emission tomography (PET) imaging using Aβ and Tau tracers demonstrated that patients with Lewy body (LB) diseases manifest a spectrum of AD pathology.[9,10] Actually, a fragment of α-Syn, called the non-Aβ component (NAC), was originally identified in samples containing Aβ plaques.[11] A growing body of evidence supports that Aβ enhances α-Syn pathology. For instance, the existence of AD pathology accelerates Lewy pathology and the progression of DLB.[12,13] Accumulation of p-α-Syn is enhanced in double transgenic mice with mutant APP and presenilin-1.[14]

Brain imaging scans are excellent tools to assist in the diagnosis of PD and rule out other potential causes of motor disorders. When combined with a detailed history and physical examination, they enable physicians to make a diagnosis with high probability. α-Syn is a valuable imaging target for PD because α-Syn deposition in LBs and Lewy neurites (LNs) in the substantia nigra (SN) and elsewhere in the brain distinguishes PD from other atypical parkinsonisms, including progressive supranuclear palsy (PSP) and corticobasal degeneration (CBD), and is the defining feature for postmortem pathologic diagnosis.[15] Although a variety of imaging techniques are available, including PET, single photon emission computed tomography (SPECT), and magnetic resonance imaging (MRI), they have not been useful as sensitive, specific, and reliable biomarkers for the presence and progression of PD. Thus, a small molecular PET radiotracer with high affinity and selectivity to fibrillar α-Syn could be useful to quantify the levels of α-Syn aggregation non-invasively. The density of α-Syn aggregates in PD brains is lower than that of Aβ and Tau in AD brains. Thus, it is more challenging to develop specific PET tracers for α-Syn.[16] To date, no useful α-Syn PET tracer has been identified, although advances have been made in this field.[16-18] Current diagnostic PET radioligands for PD target either the dopaminergic system (pre-synaptic and post-synaptic dopamine activity) or vesicular monoamine transporter type 2 (VMAT2).[19,20] Unfortunately, such imaging strategies are unable to distinguish PD from atypical parkinsonisms that also result in the degeneration of nigrostriatal projections.[21,22] In addition, dopaminergic medications used for symptomatic treatment may alter striatal uptake of these agents, limiting their reliability for measuring disease progression.[23,24]

An imaging biomarker would be extremely useful for diagnosis and drug development as an outcome measure in clinical trials. LB imaging would enable early, more accurate diagnoses, along with monitoring of disease progression, in a range of clinical conditions, including PD, DLB, MSA, PSP, etc. To address these urgent clinical needs, we have prioritized α-Syn imaging as the most likely imaging approach to have an impact on therapeutic development. The rationale behind our approach is that imaging the key pathological feature of PD would be the most direct and, hopefully most sensitive means of measuring the progression of disease and the effectiveness of therapeutics. In scrutinizing the literature regarding α-Syn binding ligands, we noticed some common molecular structure features for targeting α-Syn. Accordingly, we screened and synthesized a series of molecular derivatives and performed *in vitro* α-Syn, Aβ, and Tau fibril binding assays. The top structural backbones were further optimized via organic synthesis, followed by counter screenings using *in vitro* fibrils and in

primary neurons with these aggregates; binding assays were performed with brain sections containing LBs, Aβ-enriched senile plaques, and NFTs with hyperphosphorylated Tau as the major components. Finally, a novel benzothiazole-ethenyl-phenol derivative (F0502B) was obtained. The [^{18}F] fluorinated F0502B specifically recognized α-Syn fibrils *in vitro* and *in vivo*. It selectively labeled α-Syn inclusions in the brains of non-human primates. Our cryoelectron microscopy (cryo-EM) structure of α-Syn fibrils in complex with F0502B further provides atomic details for the binding of F0502B with α-Syn fibrils and suggests in general how small compounds bind amyloid fibrils with high affinity and selectivity. Therefore, our study reveals a promising lead compound for imaging α-Syn and facilitating the diagnosis of synucleinopathies. This might provide a tool to improve the understanding of disease progression and potentially monitor therapeutic efficacy in clinical trials.

RESULTS

PET tracer chemical design and screening strategy

Numerous small molecules bind to α-Syn and inhibit its aggregation. For instance, a polyphenolic moiety in both dopamine (or polymers containing dopamine) and baicalein potently inhibits α-Syn aggregation,[25-27] suggesting that catechol groups may influence molecular binding to α-Syn. In addition, the backbones of melanin or eumelanin, two dopamine metabolites, are structurally homologous to the benzothiazole group in the Aβ PET tracer Pittsburgh compound-B (PiB) or benzothiazine in a reported α-Syn radioligand.[28] These findings led us to investigate whether introducing hydroxyl groups onto the benzothiazole or benzothiazine moiety would increase their binding affinity and specificity toward α-Syn. Thus, conjugating these two functional groups via a connecting ethylene group might provide a useful core structure for α-Syn PET tracers. Additionally, the compound anle138c with a catechol group resulted in complete the inhibition of α-Syn aggregation further supporting that catechol groups might selectively bind α-Syn.[29]

The general strategy that we employed to screen the candidate α-Syn PET agents is summarized as follows: (1) perform *in vitro* binding assays with preformed fibrils (PFFs) of α-Syn and counter-screen with Tau and Aβ PFFs; (2) test the positive compounds in animal models with aggregated α-Syn, Tau, or Aβ; (3) screen with the brain slides from mice injected with virus encoding α-Syn, and counter-screen with aged 3xTg (containing both Aβ plaques and NFTs) and Tau P301S (containing NFTs) transgenic mouse brain sections; (4) screen patient brain sections from DLB and MSA against AD; (5) determine the binding kinetics between α-Syn PFFs and positive hits; (6) determine the *in vivo* brain/plasma (B/P) ratios and the brain permeability of the candidates, and (7) determine the *in vivo* PET images in rodent and non-human primate models of synucleinopathies with the final candidate (Figure 1A).

To perform the *in vitro* binding assay, we first screened 23 commercial compounds that met the desired structural requirements (Table S1, upper). The summary of the binding activities toward α-Syn PFFs and the positive control thioflavin-T (ThT) is depicted in Figure 1B. The most robust binding activities toward α-Syn PFFs were found with Z644 and Z257. Using counter screening, much higher binding was found toward α-Syn than Aβ or Tau PFFs (Figure S1A, upper). Noticeably, Z644 displayed significantly higher binding toward α-Syn

than ThT, whereas the homolog derivative Z819 interacted weakly with α-Syn PFFs (Figure S1A, lower), indicating that the presence of a phenol group might be critical for α-Syn association. The structure of PFFs was validated by electronic microscopy (EM) (Figure S1B).

Screening assays with PFFs of α-Syn, Tau, and Aβ

Consistent with the structural characteristics of our top two hits, we synthesized a series of derivatives by including an amino group and a methyl group on benzothiazole to increase brain permeability and fluorescent signals (Data S1; Table S1). The 21 derivatives subsequently underwent the α-Syn PFF binding assay and were counter-screened with Tau and Aβ PFFs. Compounds with significant α-Syn PFF binding and modest binding to Aβ or Tau PFFs are highlighted in red boxes (Figure 1C). Next, we screened these positive compounds in neuronal models containing α-Syn, Tau, and Aβ aggregates to assess their binding selectivity. Primary cultured neurons were infected with adeno-associated virus (AAV) encoding α-Syn or Tau for 7 days and then treated with α-Syn, Tau, or Aβ PFFs to induce the formation of intracellular aggregates following previously described protocols.[30] The candidate compounds were added to the primary neurons with the indicated aggregates and analyzed using fluorescence microscopy. Of these tested compounds, EU04-02A, EU04-03A, EU05-02A, EU05-01A, EU05-02B, and EU05-03B yielded positive signals in neurons with α-Syn aggregates (Figures 1D and S1C). The formation of insoluble Tau aggregates in primary neuronal cultures was confirmed by sequential extraction (Figure S1D).

Screening of positive compounds with brain sections containing α-Syn deposits

To further explore whether our candidate compounds selectively bind to α-Syn deposits, we employed brain slices from mice injected with AAVs encoding A53T mutant human α-Syn. α-Syn aggregates were found extensively in the SN of these mice. Furthermore, we tested the specificity of the compounds using Tau P301S mice with Tau inclusions that are positive for Gallyas silver staining (Figure S1E), Aβ-enriched 5xFAD mice, and 3xTg mice that possess both Tau and Aβ pathologies. The α-Syn deposits were labeled with p-α-Syn S129 antibody and were also stained with fluorescent signals from EU05-02B, which barely recognized Aβ plaques or NFTs (Figures 1E and S1F). As a positive control, thioflavin-S (ThS) stained all of these aggregates in the brain sections. Only weak signals toward α-Syn deposits were found with other compounds, although none of the tested compounds were reactive with NFTs (Figure S1G). However, both Z257 and Z644 were associated with Aβ plaques (Figures S1H and S1I). Next, we extended our *ex vivo* screening to human DLB, MSA, and AD patient samples. Again, robust signals were found to colocalize with α-Syn pathology in DLB and MSA patient brain slides stained with EU05-02B, but it did not stain Aβ plaques or NFTs in AD (Figures 1F, 1G, and S2A-S2D). Other compounds, including EU04-03A and EU05-02A, also co-stained with α-Syn deposits and barely recognized AT8-positive NFTs or Aβ aggregates in AD brains, and none of them revealed signals in control samples (Figures S2A-S2D). Based on these data, we selected these three compounds for further investigation.

Optimized EU05-02B (F0502B) selectively binds to α-Syn deposits

To test whether the compounds specifically interact with α-Syn PFFs, we conducted fluorescent titration assays and measured fluorescent emission intensities with 0.08 μM of various fibrils in the presence of 5 μM of the candidate molecules. Using a fluorescent binding assay, we found partial binding selectivity toward α-Syn PFFs versus Aβ and Tau fibrils with EU05-02B but not EU-04-03A or EU-05-02A (Figures 2A middle, S3A, and S3C). Since ^{18}F has a much longer half-life and is much more favorable than ^{11}C for clinical PET usage, we decided to label the N-methyl group on EU05-02B into the N-2-(2-fluoroethoxy)ethyl-N-methyl group and named the newly synthesized derivative F0502B (Scheme 1D). Notably, F0502B specifically bound α-Syn fibrils but poorly bound Aβ or Tau fibrils, regardless of 3R or 4R Tau (Figures 2A, right and S3B). Notably, carbamation of the phenol group completely eliminated its binding activity to all of PFFs (Figure S3D). Interestingly, substituting the hydroxyl group with the amino- or methylamino-group disrupted F0502B binding affinity to α-Syn PFFs but strongly elevated its interactions with Aβ or Tau PFFs (Figure S3E). Again, these structure-activity relationship (SAR) studies emphasize that the phenol group is required for F0502B selective binding to α-Syn aggregates.

Neuronal culture binding assays and α-Syn staining from the brain sections of SN injected with AAV-α-Syn A53T mice and MSA and DLB patients validated the specific association of F0502B with α-Syn aggregates but not Aβ plaques or NFTs from 5xFAD, 3xTg, and Tau P301S mice or AD patients (Figures 2B, 2C, and S4A-S4C). Thus, the results of *in vitro* experiments were consistent with the interpretation that F0502B had greater specificity to α-Syn aggregates than Aβ and Tau aggregates compared with EU05-02B. Hence, chemical modification with a fluorinated side chain on EU05-02B appears to enhance its binding selectivity and affinity toward aggregated α-Syn fibrils.

To ensure that F0502B meets the kinetic criteria of a good PET tracer with rapid penetration into the brain and swift washout of unbound tracer, we performed an *in vivo* pharmacokinetics (PK) study in wild-type (WT) mice with i.v. injection of 5 mg/kg F0502B. The plasma half-life of F0502B was $t_{1/2}$ = 6.9 min, with a Cl rate of approximately 33.6 L/h/kg. The brain versus plasma (B/P) ratios of F0502B concentrations increased from 0.106 at 1 min to 13.37 at 1 h (Table S2). The *in vivo* pharmacokinetic curves are summarized in Figure 2D. Thus, F0502B readily enters the brain. Accordingly, we administered 2 mg/kg F0502B via i.v. injection into WT mice infected with AAV-α-Syn A53T, 5xFAD mice, Tau P301S mice, and age-matched control mice (8 months old). 2 h later, we sacrificed the mice and stained the brain sections with anti-Aβ, anti-p-Tau (AT8), anti-p-α-Syn S129, and ThS. As a negative control, in the brains of WT mice, no p-S129 or F0502B staining signals were found. In contrast, α-Syn aggregates in AAV-α-Syn A53T-injected mouse brains stained with anti-p-S129 co-localized with both F0502B and ThS. The Aβ plaques in 5xFAD mice and 3xTg mice and Tau aggregates in 3xTg and Tau P301S mice were robustly stained by ThS but not F0502B. Thus, F0502B selectively stains α-Syn aggregates but not Aβ or Tau aggregates in AD mouse models (Figures 2E and S4D-S4F). To eliminate the potential effect of surgical procedures on F0502B staining, we performed staining with α-Synuclein protein coding gene (SNCA) transgenic mice treated with rotenone, which contains abundant LB-

like inclusions. F0502B stained the α-Syn inclusions that were positive for p-S129 and 5G4 (Figure S4G). We further performed a toxicology test and found that F0502B did not alter complete cell count or liver/renal functions in C57BL/6 mice (Table S3). Hence, the *in vivo* data with non-radiolabeled F0502B demonstrated selective binding to α-Syn aggregates in PD mouse models but no binding to ThS-positive Aβ or Tau aggregates in AD mouse models.

Quantification of F0502B interaction with α-Syn fibrils versus Aβ and Tau fibrils

To further characterize F0502B, we developed a rapid ^{18}F-radio-labeling route with high yield (Scheme 1E). Binding assays to α-Syn, Tau, and Aβ PFFs were conducted to validate their specificities. The binding data were analyzed by curve fitting using nonlinear regression to obtain dissociation constant (K_D) and maximal number of binding sites (B_{max}) values (summarized in Figure 3A). These values defined the specific binding affinity with different fibrils. The affinity of [^{18}F]-F0502B to $Aβ_{1–42}$ or Tau fibrils was much lower than that for α-Syn fibrils (α-Syn fibrils K_D: 10.97 nM, Aβ fibrils K_D: 109.2 nM, Tau fibrils K_D: 120.5 nM) (Figure 3A). The competitive binding assay utilizing fixed concentrations of α-Syn fibrils and [^{18}F]-F0502B showed that [^{18}F]-F0502B was selectively displaced by increasing concentrations of cold F0502B but not EU03-01B (Figure 3B). To determine whether a binding site identified on recombinant α-Syn fibrils is also present in PD tissues and test whether the density of binding sites is high enough to image fibrillar α-Syn *in vivo*, we conducted [^{18}F]-F0502B binding to PD/AD/WT mice and PD/DLB/AD patients/healthy control brain homogenates and extracted α-Syn, Tau, and Aβ insoluble fibrillar fractions prepared from these samples (Figures 3C-3F). Noticeably, the binding curves for total and nonspecific (NS) binding for [^{18}F]-F0502B in the PD/AD/healthy control tissues showed only specific binding with PD tissues but not AD or control tissues (Figure 3G). The K_D and B_{max} values for aggregated α-Syn in PD patients were 3.68 nM and 14.95 fmol/nmol, and those for DLB patients were 6.23 nM and 12.30 fmol/nmol, respectively. In contrast, K_D and B_{max} values for Aβ fibrils in AD patients were 107.80 nM and 2.34 fmol/nmol, respectively, and those for Tau fibrils in AD patients were 151.20 nM and 1.14 fmol/nmol, respectively (Figure 3E). We also validated AD patient brain samples with ^{18}F-AV1451 and ^{18}F-AV45, which contained abundant Aβ plaques and NFTs (Figure S3F). These results indicate that [^{18}F]-F0502B binding affinity in PD or DLB brains is comparable with the binding affinity for aggregated α-Syn from SNCA A53T transgenic mice treated with rotenone or mice injected with AAV-α-Syn A53T but more potent than that for recombinant α-Syn fibrils. F0502B also competed well against [^{3}H]BF227, a previously reported α-Syn radioligand,[31] in binding to aggregated α-Syn in PD brains with a K_i value of 3.4 nM. Thus, F0502B specifically interacts with α-Syn fibrils.

[^{18}F]-F0502B specifically binds α-Syn aggregates in human PD brains

Autoradiography with human brain slices showed that [^{18}F]-F0502B selectively associated with LBs in brain sections from PD but not AD patients. The binding activities were blocked by excessive cold F0502B (Figures 4A and 4B). To ascertain whether the specific binding truly reflected the pathology of the target of interest, we performed immunohistochemistry staining with adjacent brain tissue slices. pS129 staining revealed abundant LBs in both the midbrain and amygdala from PD brains, fitting with robust ^{18}F radioligand binding patterns.

Although anti-Aβ and AT8 stainings were strong in AD brains, pS129 was barely detectable in AD or healthy controls, correlating with their negligible binding activities (Figure 4A, right). Together, these findings support that F0502B specifically and avidly binds to α-Syn fibrils in LBs.

Structure determination of the α-Syn fibril-F0502B complex

We next sought to determine the atomic structure of α-Syn fibril in complex with F0502B by utilizing helical reconstruction in the RELION software.[32] Although the fibrils were prepared under the same conditions as the previously reported α-Syn polymorph 1a fibril,[33] to avoid experimental bias between different batches of fibril preparation, we in parallel determined the structure of the α-Syn fibril from the same batch but without the addition of the ligand (apo-α-Syn fibril). Reference-free 2D classifications revealed that the addition of F0502B causes negligible changes to the helical parameters and 2D class average patterns of the α-Syn fibrils in comparison with the apo-α-Syn fibril (Figures S5A and S5B; Table S4). After 3D classification and helical reconstruction, we obtained the density maps of the α-Syn fibril-F0502B complex and the apo-α-Syn fibril at an overall resolution of 2.6 and 2.8 Å, respectively (Figures 5A, S5C, and S5D; Table S4). Consistent with the polymorph 1a fibril,[34] the fibril prepared in this work is composed of two identical protofilaments intertwining along an approximate 2_1 screw axis with a left-handed helix (Figures 5B, S5A, and S5B). Strikingly, we observed two stripes of additional strong densities accommodating in a deep groove of each protofilament in the complex fibril compared with the apo fibril (Figures 5A, 5B, and S5B), suggesting that these extra densities correspond to the F0502B ligand. In each strip, the additional densities separate into rungs, expanding obliquely across three successive layers of α-Syn rungs and stacking along the fibril axis (Figure 5B).

Structural model of the complex fibril and interactions between the stacking ligands

The high-resolution density map enabled us to unambiguously build a structural model for the α-Syn fibril-F0502B complex (Figure 5C). The structure of α-Syn in the complex fibril is nearly identical to that in polymorph 1a except for the terminal regions (Figure S5E).[34] Remarkably, the complex fibril contains clear densities of F0502B molecules (Figure 5D) that insert into a deep cavity on the fibril surface constructed by residues K80-E83 and Y39-E46 with its phenol head residing inward and the fluoro tail pointing outward (Figures 5E and 5F). The binding of F0502B stabilizes the N terminus of α-Syn in the fibril, which leads to clearer densities of α-Syn residues at the N terminus (Figure 5A) and induces the conformational change of Tyr39 to adapt to the ligand binding (Figure S5F).

In the ligand-binding cavity, which is actually a long, narrow channel, F0502B molecules stack along the fibril axis in parallel with each other (Figure 5E). The aromatic ring of the phenol group and the planar benzothiazole-ethenyl group are nearly in the same plane with a small twist of ~10° in each F0502B molecule (Figure 5D) and form edge-to-face π-π interactions among F0502B molecules (Figure 6A).[35] The plane of the aromatic rings is approximately diagonal (~50°) to the fibril axis (and the plane of α-Syn layers as well) (Figures 5E, 6A, and S6A). Correspondingly, the distance between the intermolecular aromatic rings of F0502B is ~3.7 Å rather than the 4.8-Å spacing between α-Syn layers (Figures 6A and S6A), which enables a more favorable distance of π-π interactions and thus

stabilizes the ligand packing.[35,36] In contrast, the fluoro tail of F0502B swings ~50° away from the benzothiazole-ethenyl plane, parallel to the α-Syn layers, and spaces 4.8 Å from each other (Figures 5D, 6A, and S6A).

Interactions between F0502B and α-Syn fibrils

In addition to self-interactions between the stacking F0502B molecules, F0502B forms robust interactions with α-Syn (Figures 6B and S6B). One F0502B expands over three stacking α-Syn molecules (i, i+1, and i+2). Its phenol head forms a typical T-shaped π-π interaction with the phenol side chain of $Tyr39_{i+1}$ with a distance of ~3.5 Å and an angle of 64° between the aromatic rings (Figure 6C).[35] As well, the benzothiazole body of F0502B forms T-shaped π-π interaction with $Tyr39_{i}$ with a distance of ~3.7 Å and an angle of 58° between the aromatic rings (Figure 6C).[35] On the other side, the phenol head forms anion-π interaction with $Glu46_{i+1/i+2}$ (Figure 6D).[37] In addition, the hydroxyl group of the phenol head forms hydrogen bonding interaction with the backbone of $Gly41_{i+1/i+2}$ (Figure 6E); meanwhile, $Glu46_{i+2}$ forms charge interactions with $Lys80_{i+2}$ (Figure 6D), which together strengthen the anion-π interaction between α-Syn and F0502B.

Apart from the π interactions, the bromine on the phenol head of F0502B forms halogen-oxygen interaction with the hydroxyl group of the side chain of $Thr44_{i+1/i+2}$ (Figure 6E).[38] The methyl group on benzothiazole forms hydrophobic interactions with $Val82_{i/i+1}$ (Figure 6F). The fluorine on the tip of the tail forms halogen bonding interaction with $Glu83_{i+1}$ (Figure 6F).[38] Notably, since F0502B repetitively aligns with α-Syn layers at a 1:1 ratio, all these interactions with α-Syn establish an intense noncovalent bonding network extending along the fibril axis (Figure S6C). Importantly, we noted that although the structures of the *in vitro* α-Syn fibrils and *ex vivo* fibrils from MSA are different,[39,40] they share a similar cavity for F0502B binding (Figures S6D and S6E). This common ligand-binding cavity may explain our observation that F0502B binds to α-Syn aggregates in the brain sections of patients with MSA (Figure 2C).

In vivo PET imaging with [^{18}F]-F0502B in non-human primate models of PD

To further evaluate the diagnostic ability of the PET tracer, we established two non-human primate models of PD by injecting α-Syn PFFs or AAV-α-Syn A53T into the striatum of rhesus macaques.[41,42] One and a half years later, PET scans demonstrated that both monkey models displayed significantly reduced dopamine transporter (DAT) signals in the striatum when compared with control monkeys, indicating that both AAV-A53T-α-Syn and α-Syn PFFs induce nigrostriatal degeneration, which is characteristic of PD patients (Figures S7A and S7B). [^{18}F]-F0502B PET scan revealed demonstrable signals in the striatal regions in monkey brains injected with AAV-α-Syn A53T. Similar PET imaging results were observed in the striatum of α-Syn PFF-injected monkeys. In contrast, the brains of control monkeys were devoid of radiotracer retention (Figures 7A-7C; Video S1). To obtain better overlay images for the control monkey brain, we have edited out the extracerebral tissues and scaled the image to the highest intracerebral standardized uptake value (SUV) in the brain, which clearly showed much higher signals in the PFF- and virus-injected groups than the control group. The T1-weighted images and PET images were co-registered using PMOD

software (Figure S7C). These promising results support further research and development of [^{18}F]-F0502B as a PET tracer of potential utility in imaging synucleinopathies *in vivo*.

DISCUSSION

In this study, we identified a novel benzothiazole-ethenyl-phenol derivative (F0502B) that displayed a K_D of 4.26–7.32 nM for α-Syn deposits in PD brains. The [^{18}F]-labeled F0502B specifically bound with high affinity to α-Syn fibrils over Aβ and Tau fibrils. F0502B selectively labels α-Syn aggregates in mouse and monkey PD models. The *in vivo* PK studies demonstrated that F0502B possesses favorable brain permeability and is washed out of the normal brain swiftly. As described previously,[43,44] useful neuroimaging radiotracers should possess the following chemical and pharmacological properties: high brain-blood barrier (BBB) permeability, rapid clearance from normal brain tissue and blood, and high-affinity binding and high binding selectivity for the target. Together, our studies demonstrate that F0502B meets these criteria. *In vivo* PET imaging shows that [^{18}F]-F0502B specifically recognizes α-Syn aggregates in monkeys. Remarkably, it neither associates with the Aβ plaques in aged 5xFAD and 3xTg mice nor the Tau aggregates in aged 3xTg mice or Tau P301S mice. It is possible that aggregated α-Syn levels in the two non-human primate PD models could increase over time, resulting in elevated PET-specific binding signals. Nonetheless, our findings demonstrate that F0502B acts as a specific PET tracer by selectively binding to aggregated α-Syn.

Several compounds are currently under investigation for imaging α-Syn deposits. The ^{18}F-labeled compound BF-227 ((aminothiazolyl-ethenyl)-benzoxazole derivatives) binds to both synthetic α-Syn aggregates and Aβ fibrils *in vitro*.[31] A PET study with ^{11}C-labeled BF-227 showed its ability to detect α-Syn deposits in the living brains of patients with MSA.[45] However, the high affinity of this radiotracer for Aβ plaques limits its usefulness in humans for differential diagnosis. The selectivity of other phenothiazine derivatives against α-Syn versus Aβ and Tau is not optimal for imaging α-Syn *in vivo*.[28,46] The *in vitro* characterization of (benzylidene) indolin-2-one derivatives as ligands for α-Syn fibrils with high affinity and selectivity for α-Syn has been reported, but these compounds have not yet been translated to human imaging applications.[47] Structurally, BF-227 and F0502B share some homology on the benzoxazole (benzothiazole)-ethenyl portions of the molecules. The competition assay of [^{3}H]BF-227 with F0502B in postmortem PD patient brain tissue containing α-Syn aggregates revealed a Ki of 3.4 nM. Mounting evidence supports the role of phenol or catechol groups in promoting interaction with α-Syn-containing species.[48,49] This could help explain the nonselective binding of BF-227 to both Aβ and α-Syn aggregates,[31] whereas F0502B exhibited specificity in binding aggregated α-Syn. Extensive SAR study supports that the phenol group in F0502B is required for its binding properties, and carbamation of this group abolishes its activity (Figure S3D). This SAR is consistent with a previous report that compounds with a catechol group (anle138c) displayed strong inhibition of α-Syn aggregation, whereas it has little effect on prion aggregation, further supporting the importance of the catechol group in F0502B selectively interacting with α-Syn. Moreover, methylation of the catechol group substantially diminishes its inhibitory activity against α-Syn aggregation (sery255b), suggesting that alkylation of the catechol group might decrease its interactions with α-Syn.[29] Strikingly, replacing the OH group

with amino- or methylamino- group completely abolishes F0502B binding activity to α-Syn PFFs. In contrast, these modifications augment the binding affinity to Aβ or Tau PFFs (Figure S3E). Conceivably, the dimethylamino group on BF227 may be accountable for its high affinity toward Aβ fibrils, sabotaging its specificity to α-Syn fibrils.

The cryo-EM structure of an α-Syn fibril complexed with F0502B provides a structural basis for F0502B's binding to aggregated α-Syn. It was believed that the binding of small molecules to amyloid fibrils was nonspecific, which was, at least in part, attributable to the nonselective binding of some dyes to a variety of amyloids[50-54] and also due to the low densities of amyloid ligands bound to fibrils.[55] The present structure demonstrates that α-Syn fibrils may have defined cavities for specific binding of small molecules, similar to the binding of ligands to native proteins. However, fundamental differences exist between the binding of small molecules to native proteins and amyloid fibrils. Some native proteins have well-defined 3D pockets for ligand binding. In contrast, the ligand-binding pocket of amyloid fibrils may be constrained to two dimensions that are formed along the fibril growing axis, thereby resulting in a ligand-binding channel or groove. Confining the ligand-binding sites to those along the fibril axis would likely strongly influence specific fibril-ligand-binding interactions. This detailed α-Syn fibril structural information could aid in a structure-based rational design and optimization approach to develop more potent α-Syn PET tracers.[56,57] Since both LBs and LNs are formed by α-Syn fibrils, F0502B may not be able to differentiate them.

In addition, structural differences that may exist between synthetic *in vitro* and *ex vivo* (human-derived) amyloid fibrils have been discussed with respect to their influences on drug development.[34,40,58] *Ex vivo* human-derived fibrils are too limited to be applied in large screening assays. Our study demonstrates a strategy for PET tracer design by targeting potential conserved binding sites shared by *in vitro* and *ex vivo* fibrils, which appears to be a successful strategy applied in the development of F0502B. A similar strategy could also be considered for high-throughput screening and optimization of amyloid tracers for other neurodegenerative diseases. It is worthwhile to note that although the *in vitro* α-syn fibril structure is quite different from the lately reported Lewy fold structure of α-syn fibrils extracted from PD and DLB brains,[59] residues Y39-E46 that compose the F0502B binding pocket are also involved in the composition of a pocket on Lewy fold that is naturally occupied by unidentified molecules (Figure S6F). This, on the one hand, indicates the importance of these molecules in the Lewy fold formation and on the other hand may indicate a potential pocket of Lewy fold for drug development. At the same time, it is also hard to ignore that Lewy fold occupies only ~25% of the total extracted α-syn fibrils.[59] To this point, although direct structural evidence for F0502B binding to Lewy fold is currently lacking, its ability of binding to PD/DLB fibrils cannot be excluded. Actually, our biochemical and imaging data support the binding of F0502B to PD/DLB fibrils in patient brains. In addition, F0502B may not be able to differentiate LBs and LNs since both contain α-Syn fibrils.

Our *in vitro* binding assays demonstrated that F0502B selectively interacts with α-Syn over Aβ or Tau fibrils. F0502B specifically binds to α-Syn deposits in both MSA and DLB patient brain sections but not to Aβ plaques or NFTs in AD patients that were

ThS-positive (Figure 2). Although F0502B exhibits faint signals on AD patient sections, they are not co-localized with signals from Aβ plaques or NFTs. The planar benzothiazole-ethenyl group conjugated with phenol could help define F0502B's spatial and chemical selectivity for aggregated α-Syn. This is supported by the X-ray crystallography analysis of the planar conformation of F0502B (Table S5). Although F0502B is weakly associated with Aβ aggregates in 5xFAD brain sections *in vitro*, it selectively stained α-Syn deposits in PD mouse brains over Aβ inclusions in 5xFAD brains (Figure S4A). Imaging the key pathological feature of PD would be the most direct and possibly the most sensitive means of measuring the progression of disease and the effectiveness of therapeutics that alter disease progression. Hence, this radioligand might have imaging applications in different synucleinopathies and potentially help to monitor the effects of disease-modifying treatments. Successful α-Syn imaging will likely assist in therapeutic drug development for these diseases.

Limitations of the study

Here, we have identified that F0502B specifically binds to α-Syn aggregates and may be used as a PET tracer for the diagnosis of synucleinopathies. It should be noted that this promising lead compound may need further refinement before it can be used for the clinical diagnosis of PD. F0502B interacts with α-Syn aggregates in postmortem brain sections, but it remains unknown whether it is useful to image α-Syn aggregates in patients. Our cryo-EM data shows that F0502B binds across three layers of α-Syn molecules in recombinant α-Syn protofilament. The recombinant α-Syn fibrils are structurally different from fibrils in the human PD brain. The cryo-EM structure of F0502B binding with human brain-derived α-Syn fibrils should be studied in the future. Finally, although we found that this compound specifically binds to α-Syn fibrils, its potential off-target effect should be further tested in animal models and PD patients.

STAR★METHODS

RESOURCE AVAILABILITY

Lead contact—Further information and requests for resources and reagents should be directed to and will be fulfilled by the lead contact, Keqiang Ye (kq.ye@siat.ac.cn).

Materials availability—All unique reagents generated in this study are available from the lead contact upon reasonable request. We may request the completion of a Materials Transfer Agreement and request reasonable compensation by the requestor for material processing and shipping.

Data and code availability

- The cryo-EM map data has been deposited in the Electron Microscopy Data Bank (EMDB) under accession numbers EMD-32615 for α-Syn fibril-F0502B complex. The corresponding atomic model has been deposited in the Protein Data Bank (PDB) under the accession number 7WMM. The structural models used in this study are available in the PDB database under accession codes 6A6B (apo-α-Syn fibrils), 6XYO (MSA type I), 6XYP (MSA type II1), 6XYQ (MSA

type II2), and 8A9L (Lewy fold), respectively. These data are publicly available as of the date of publication, DOIs are listed in the key resources table. All data reported in this paper will be shared by the lead contact upon request.

- This paper does not report original code.
- Any additional information required to reanalyze the data reported in this paper is available from the lead contact upon request.

EXPERIMENTAL MODEL AND SUBJECT DETAILS

Primary cells—Primary rat cortical neurons were cultured as previously described.[24] All rats were obtained from the Jackson Laboratory. The protocol was reviewed and approved by the Emory Institutional Animal Care and Use Committee. Cells were incubated at 37 °C in a humidified atmosphere of 5% CO_2. The Sprague-Dawley rats were used at embryonic E18 days, the cortical tissue was isolated, dissociated, and incubated with 5 ml of D-Hanks containing 0.25% trypsin for 5 min, centrifuged at 1000 × g for 5 min after addition of 4 ml of the neuronal plating medium containing DMEM/F12 with 10% fetal bovine serum. The 1 x 10^5 cells were plated in 6-well plates for further process. DIV7 neurons were infected with AAV-Tau or AAV-α-Syn. On DIV12, the neurons were transduced with Tau, α-Syn or Aβ PFFs. Sonicated PFFs, or an equivalent volume of the monomer as a control, were transferred into pre-warmed neuronal medium at a final concentration of 100 ng/ml. The method was similar to that reported previously.[30]

Mice—Wild-type C57BL/6J mice and Tau P301S, 3xTg and 5xFAD mice were ordered from the Jackson Laboratory (stock numbers: 000664, 008169, 034830, 034848). Animal care and handling were performed according to the NIH animal care guidelines and Emory Medical School guidelines. The protocol was reviewed and approved by the Emory Institutional Animal Care and Use Committee. Both male and female mice were used. Animals were equally divided into groups for each sex. For brain immunofluorescence, the brain slices from 14-month-old 3xTg mouse cortex, 6-month-old Tau P301S mouse cortex, and 12-month-old 5xFAD mouse cortex were used. For F0502B *ex vivo* assay, eight-month-old wild-type, 5XFAD, Tau P301S, 3xTg and AAV-α-Syn A53T-injected mice were injected with F0502B via the vena caudalis at 2 mg/kg. Brain sections were prepared 2 h after injection.

Rhesus macaques—Rhesus macaques were ordered from Hubei Topgene Biotechnology Co., Ltd. The experiment was approved by the Institutional Animal Care and Use Committee at Tongji Medical College, Huazhong University of Science and Technology. Eight laboratory-bred female rhesus macaques were 4-5.5 years old and weighed 4-6 kg at the start of the experiment. Two monkeys received injections of PBS, three received AAVs encoding A53T mutated human α-Syn, and three received α-Syn PFFs. Anatomical magnetic resonance imaging (MRI) was performed on each animal to derive surgical coordinates. The surgery was conducted under Shu-Mian-Ling II injection anesthesia (0.06 ml/kg combined with 0.05 mg/kg atropine, i.m., add 1/3-1/2 dose every hour) (Laboratory of Small Animal Diseases, Nanjing Agricultural University, China) under sterile conditions. Precise stereotaxic coordinates for all surgeries were calculated from the MRI of each

monkey using 3D Slicer software. Each of the three sites in the right putamen was injected with 3 μl of rAAV (1.18 X 10^{13} vg/ml) or 40 μl α-Syn PFFs (5 mg/ml). The injections were made at a rate of 2 μl/min by using a 26-gauge Hamilton microsyringe that was left in place for an additional 5 min after each injection. After surgery, the monkeys were immediately given an analgesic (Tramadol hydrochloride injection, 3 mg/kg, i.m.) and antibiotic (gentamicin, 10 mg/kg, i.m., for 3 days). Animals were kept warm in an incubator until they were well enough to be returned to their home cage.

Human samples—Post-mortem brain samples were dissected from frozen brains of AD, DLB, MSA patients and age-matched control subjects from the Emory Alzheimer's Disease Research Center. The Biospecimen Committee approved the study. AD, DLB, and MSA were diagnosed according to the criteria of the Consortium to Establish a Registry for AD, DLB, MSA and the National Institute on Aging. The patients' information is summarized in Table S6.

METHOD DETAILS

Screening candidate compounds with fibril binding assay—The candidate compound solution (5 μM) in binding buffer (50 mM Tris-HCl, 50 mM NaCl, pH 7.4) was added into each of three wells containing α-Syn, Aβ, Tau fibrils or their monomers (0.08 μM) in Tris-HCl buffer (50 mM, pH 7.4) in a 96-well plate to make a reaction volume of 200 μL for fluorescence detection. α-Syn fibrils were purchased from Proteos. Inc. (RP-002) and dissolved in PBS to a final concentration of 1 mg/ml. Tau and Aβ fibril preparations are described below. The reaction plate was determined according to each compound's characteristic excitation (Ex) and emission (Em) wavelengths by a BioTek fluorescence plate.

***In vitro* saturation binding assays to determine the binding affinity of EU0502B for fibrils—**A fixed concentration of EU05-02B (0.5 μM) was incubated for 2 h at 37 °C with increasing concentrations of α-Syn, Aβ or Tau fibrils (0.08-2.56 μM) in binding buffer (50 mM Tris-HCl, 50 mM NaCl, pH 7.4) to make a reaction volume of 150 μL. Nonspecific binding was determined in a triplicate set of binding reactions containing the same concentration of EU0502B with no fibrils. Fluorescence was determined in a Biotek plate reader using a 440/30 excitation filter and a 528/20 emission filter. Thioflavin T (0.5 μM) was used as a positive control to confirm the quality of recombinant fibrils by using a 440/30 excitation filter and a 485/20 emission filter. The saturation binding curve and K_d value were analyzed using GraphPad Prism 7.0.

EU0502B and F0502B fluorescence measurement—Fluorescence measurements of EU05-02B and F0502B in combination with α-Syn, Aβ or Tau fibrils were performed in fused silica cells (Hellma, 10 x 4 mm, Typ 117.04F-QS) with a fluorescence spectrometer (Horiba Fluorolog3) equipped with an anisotropy module (FL-1044). EU0502B and F0502B were first dissolved to 10 mM in DMSO and then directly diluted to 50 μM in binding buffer (50 mM Tris-HCl, 50 mM NaCl, pH 7.4). Two hundred microliters of this diluted solution was filled in cuvettes with the indicated concentration of fibrils. After incubation for 1 h, the

solution was excited at a wavelength of 386 nm, and the emission spectrum was acquired at 510 nm with both excitation and emission slit widths of 5 nm.

Stereotaxic injection—AAV9-α-Syn A53T was injected into the substantia nigra of 3-month-old wild-type C57BL/6J (n = 15) mice. The rodents were anesthetized with isoflurane (Piramal Healthcare). Meloxicam (Loxicom; 2 mg/kg) was injected s.c. for analgesia. Unilateral intracerebral injection of AAVs was performed stereotaxically at the following coordinates: for mice, anteroposterior −3.2 mm and mediolateral −1.3 mm relative to bregma and dorsoventral −4.3 mm from the dual surface. Two microliters of viral suspension were injected into each site using 10-μL glass syringes with a fixed needle at a rate of 0.25 μL/min. The needle remained in place for 5 min after the virus injection was completed and then was removed slowly (over 2 min). The rodents were placed on a heating pad until they began to recover from anesthesia.

Immunofluorescence—The cells or brain slices were fixed and incubated for 12 h at 4 °C with primary antibodies followed by incubation with Alexa Fluor 568-, Alexa Fluor 488-, or Alexa Fluor 647-conjugated secondary antibodies (Invitrogen) for 3 h at room temperature. 4′,6-Diamidino-2-phenylindole (DAPI, 1 μg/ml) (Sigma-Aldrich) was used for the nuclear staining. The slides were imaged with Olympus FluoView FV1000 confocal laser scanning microscope using Olympus FluoView software to acquire data.

Immunohistochemistry—For immunohistochemical staining, deparaffinized and antigen-retrieved 20 μm-thick human brain sections were treated with 0.3% H_2O_2 at room temperature for 10 min. Subsequently, the sections were washed in PBS with 0.3% Triton X-100 3 times and then blocked with 1% BSA for 30 min, followed by overnight incubation with anti-Aβ/AT8/α-Syn pS129 antibody at 4 °C. The signal was developed using a Histostain-SP kit. After washing, the sections were covered with a glass cover using mounting solution.

Gallyas silver staining—Silver staining was performed as previously described.[65] Brain sections (5 μm thick) were deparaffinized in xylene and rehydrated in graded ethanol. The sections were incubated in 5% periodic acid for 5 min, washed in water, and then placed in alkaline silver iodide solution (containing 1% silver nitrate) for 1 min. The sections were then washed in 0.5% acetic acid for 10 min, placed in developer solution for 15 min, washed with 0.5% acetic acid and water. The sections were then treated with 0.1% gold chloride for 5 min and washed in water. Finally, the sections were incubated in 1% sodium thiosulphate for 5 min before a final wash.

Transmission electron microscopy (TEM)—The TEM screening was conducted as previously described.[66] The PFF samples (5 μL) were deposited on Formvar-coated 400 mesh copper grids, fixed with 0.5% glutaraldehyde, negative stained with 2% uranyl acetate (Sigma-Aldrich, Germany) and screened by CM-10 TEM.

Oral gavage of rotenone—The rotenone o.g. treatment was conducted as previously described.[66] Mice were treated with 0.1 mL/25 g of vehicle containing 1% methylcellulose (Sigma, Cat# M0512) and 1.25% chloroform (Sigma, Cat# 2432) or a solution containing

0.625 mg/mL of rotenone (ULTRA Scientific, Cat# PST-890) with 1% methylcellulose and 1.25% chloroform. We prepared rotenone solution by dissolving rotenone in chloroform and then diluting into 1% methylcellulose solution while mixing vigorously. Rotenone or vehicle control was orally administered with a 1.2 × 60 mm gavage (Unimed, Switzerland) once a day for 5 days/week, consecutively for 3 months.

Purification of recombinant Tau—Tau cDNAs were subcloned into the Not I and Sal I restriction sites of the bacterial expression vector with a GST tag, and expressed in BL21 (DE3). Bacterial pellets were resuspended in high-salt buffer (0.75 M NaCl, 50 mM Tris, pH 7.4, 1 mM EDTA) containing a mixture of fresh protease inhibitors, sonicated to 25% power for 3 min on ice 3 times, and centrifuged at 70,000 x g for 30 min. The supernatants were applied onto a glutathione sepharose bead column (GE Healthcare) and purified by GST tag. Thrombin was used to remove the GST tag. The protein was dialyzed against 100 X volume of FPLC buffer (50 mM NaCl, 50 mM Tris-HCl pH 7.4). The protein was filtered through a 0.22 μm syringe filter and analyzed using FPLC (Superdex 200 column; GE Healthcare). The purification of Tau was analyzed by SDS-polyacrylamide gel electrophoresis (PAGE) and Coomassie blue staining. Protein concentration was determined using the Bradford protein assay (Pierce) and bovine serum albumin as a standard.

Generation of pre-formed fibrils (PFFs)—α-Syn fibrils were purchased from Proteos. Inc. (RP-002) and dissolved in PBS to a final concentration of 1 mg/ml. Tau PFFs were prepared in reactions (500 μL per tube) containing 3 mg/mL Tau recombinant protein and 12.5 μM heparin in assembly buffer (50 mM Tris/50 mM NaCl, pH 7.4). The samples were incubated for 7 days at 37 °C with orbital shaking at 300 rpm until the samples appeared cloudy. The fibril conformation was confirmed by ThT binding assay. To prepare 3R-4R mixed Tau fibrils, equal amount of 0N3R and 2N4R Tau (final concentration: 1.5 mg/ml each) was incubated as mentioned above. For Aβ PFF preparation, Aβ (1-42) peptide (rPeptide, #A-1163-1) was resolved in 9 volumes of ice-cold distilled water and vortexed occasionally. After 30 min, one volume of 10X fibril-forming buffer (0.2 M NaPi, 1.5 M NaCl, 0.2% NaN_3, pH 7.5) was added. The final concentration of peptide was 1 mg/ml (220 μM). The solution was incubated at 37 °C for one week and vortexed daily. Fibril formation was verified using ThT binding assay.

Extraction of insoluble Aβ from human brain tissue—Insoluble Aβ extraction from autopsied AD human brains was performed as previously described.[67] Briefly, gray matter (60 g) was homogenized in 5.5 vol of 0.32 M sucrose, then the homogenates were sieved by slight vacuum through 100 and 200 mesh nylon cloth filters. The fraction was brought to 1 M sucrose and centrifuged at 1,700 x g for 10 min, followed by centrifugation at 4,800 x g for 30 min. The glass bead chromatography was substituted with digestion for 16 h at 37°C with collagenase/dispase (2 mg/ml) in 50 mM Tris, pH 7.2, and 0.1% NaN_3. The pallet was suspended in 1 M sucrose and homogenized, and the suspension was layered over a discontinuous density gradient of 1.8, 1.2, 1.15, 1.1 and 1.05 M sucrose in tubes. The tubes were centrifuged at 4,800 x g for 50 min. The floating pad was removed and discarded. The layer banding at 1.2-1.8 M sucrose interface, and the pellet was resuspended in ddH_2O and recentrifuged to remove sucrose.

Fluorescence measurement of candidate compounds—The excitation wavelength of each compound with intrinsic fluorescence was measured using a spectrofluorometer (Horiba, Fluorolog3). Compounds (5 μM) in 50 mM Tris-buffer (pH 7.0) containing 0.0025 % (v/v) DMSO was added to the cuvette. Then PFFs (0.02, 0.04, 0.08, 0.16, 0.32, 0.64, 1.28 μM) or monomer (1.28 μM) was added and incubated for 5 min, total volume is 200 μM. the excitation wavelength, fluorescence spectra were recorded.

Extraction of insoluble Tau from human brain tissue—Extraction of insoluble Tau was performed as previously described.[68-70] The tissues were homogenized in 10 vol of extraction buffer (10 mM Tris-HCl (pH 7.4), 0.8 M NaCl, 1mM EGTA, and 10% sucrose), and spun at 20,00 x g for 20 min. Re-extracted the pellet and recentrifuged at 100,000 x g for 30 min. The resuspended pellet (10 μl/g tissue) was further purified by 30-fold dilution in 10 mM Tris-HCl pH 7.4, 800 mM NaCl, 5 mM EDTA, 1 mM EGTA with a final concentration of 10% (w/v) sucrose, followed by centrifugation at 20,100 × g for 30 min at 4°C. The pellet, containing large contaminants such as collagen, was discarded. The supernatant was centrifuged at 100,000 × g for 1 h at 4°C. The pellet was resuspended in 20 mM Tris-HCl pH 7.4 containing 100 mM NaCl at 10 μl/g tissue, and run over a Superose 6 Increase 3.1/300 column (GE Healthcare).

Extraction of insoluble α-Syn from human brain tissue—Extraction of insoluble α-Syn was performed as previously described.[71] Briefly, frozen PD, DLB human brain tissues were homogenized in 10 vol of cold extraction buffer (50 mmol/L Tris-HCL pH 7.4, 800 mmol/L NaCl, 10 mM NaF, 5 mmol/L EDTA) at 100,000 x g for 30 min. Re-extracted pellets with extraction buffer, followed by sequential extraction process with extraction buffer adding 1% Triton X-100 and extraction buffer with 1% Triton X-100 and 30% sucrose. The pellets were resuspended and homogenized in 1% sarkosyl extraction buffer, incubated overnight and spun at 100,000 x g for 30 min. The sarkosyl-insoluble pellets were resuspended in 50 mM Tris-HCl.

Induction of Tau or α-Syn aggregates in primary neurons—Primary hippocampal neurons were isolated from E16-17 pregnant rats. DIV7 neurons were infected with AAV-Tau or AAV-α-Syn. On DIV12, the neurons were transduced with Tau, α-Syn or Aβ PFFs. Sonicated PFFs, or an equivalent volume of the monomer as a control, were transferred into pre-warmed neuronal medium at a final concentration of 100 ng/ml. The method was similar to that reported previously.[30]

Crystals of F0502B formation—Single yellow plate-shaped crystals of F0502B were obtained by slow evaporation of MeOH. A suitable crystal of 0.45×0.20×0.05 mm^3 was selected and mounted on a loop with paratone oil on an XtaLAB Synergy, Dualflex, HyPix diffractometer. The crystal was kept at a steady $T = 101(2)$ K during data collection. The structure was solved with the ShelXT structure solution program using the intrinsic phasing solution method and by using Olex2 as the graphical interface.[72,73] The model was refined with version 2017/1 of ShelXL using least squares minimization.[73]

***In vitro* competition assay for F0502B—**The binding affinity (Ki) of F0502B was determined against [^{3}H]BF-227[31] (Moravek, Brea, CA, USA) in postmortem human PD

brain tissue (MJ Fox Foundation) with autopsy-confirmed α-Syn aggregates and no other detectable aggregated amyloid species using published methods.[74] Briefly, PD tissue was homogenized in ice-cold PBS at 300 mg/mL on ice using a glass homogenizer, diluted 30-fold with PBS to 10 mg/mL and homogenized a second time with a Brinkmann Polytron homogenizer before storage at −80 °C. Frozen PD brain tissue was thawed and diluted 10-fold in PBS/0.1% BSA to 1 mg/mL. The concentration of unlabeled F0502B (~ 400 μM in the stock solution) was determined by quantitative NMR in DMSO (0.25% DMSO in the final assay vials). The appropriate concentrations (ranging from 0.1-1000 nM) of unlabeled F0502B in 400 μL of PBS/0.1% BSA, pH 7.0 buffer, were combined with 500 μL of [^{3}H]BF-227 in buffer solution (~ 2 nM). The assay was initiated by the addition of 100 μL of 1 mg/mL PD brain tissue homogenate to achieve a final concentration of 100 μg tissue/mL. After incubation for 60 min at room temperature, the binding mixture was filtered through a Whatman GF/B glass filter via a Brandel M-24R cell harvester (Gaithersburg, MD, USA) and rapidly washed four times with 3 mL PBS/0.1% BSA buffer. The filters were counted in Cytoscint-ES after thorough vortexing using a liquid scintillation counter. Complete (100%) inhibition of specific binding was defined as the number of counts displaced by 1 μM unlabeled F0502B. All assays were performed in triplicate at each concentration.

***In vitro* binding assay for [^{18}F]-F0502B—**For the saturation binding assay, a fixed concentration (1 μM/well) of α-Syn, Aβ and Tau PFFs was incubated for 1 h at 37 °C with increasing concentrations of [^{18}F]-F0502B (5-900 nM) in 30 mM Tris-HCl pH 7.4, 0.1% BSA, and sodium ascorbate 0.5% m/v in a reaction volume of 500 μl. Nonspecific binding was evaluated with 2 μM unlabeled F0502B and 1 μM PFFs. After incubation, the mixture was filtered and vacuumed, washed twice with 600 μl washing buffer, and scintillation was counted immediately. The process was duplicated. The dissociation constant (K_d) and the maximal number of binding sites (B_{max}) values were determined by fitting the data to the equation $Y = B_{max}*X/(X+K_d)$ by nonlinear regression using GraphPad Prism software (version 7.0). B_{max} (fmol/nmol) = CPM/(2.22*10^{12} dpm/Ci *0.75 cpm/dpm * 2000 Ci/mmol *10^{-12} mmol/fmol * 0.5 nmol), the counting efficiency = 75%, and the value 2000 Ci/mmol is the specific activity of [^{18}F]-F0502B (CPM, counts per minute; dpm, disintegrations per minute). For the competition binding assay, the reaction mixture (volume: 500 μl) with 1 μM α-Syn PFFs and [^{18}F]-F0502B (half of the K_d ~ 20 nM) was added with increasing concentrations of cold F0502B (7 points, from 1/100 to 10000 X ^{18}F-0502B). The PFFs were diluted to 1 μM, and non-radio-labeled or radio-labeled F0502B was added as described above and incubated for 1 h. The mixture was filtered, vacuumed, and washed 3 times with buffer. The vacuumed samples were analyzed on a scintillation counter. The data were analyzed and calculated for Ki and IC_{50}.

Patient brain lysate binding assay for [^{18}F]-F0502B—Western blotting was performed using the pS129 antibody to analyze the levels of each case and normalize different concentrations of brain lysates to adjust the DLB/PD/AD patient aggregate concentrations (4 control and 4 DLB/PD/AD patients). The buffer used was 50 mM Tris-HCl, 50 mM NaCl, and sodium ascorbate 0.5% m/v, pH 7.4. Brain homogenates at a fixed concentration (0.2 mg/ml) were incubated for 1 h at 37 °C with increasing concentrations of [^{18}F]-F0502B (5-900 nM) in a reaction volume of 500 μl. After incubation, the mixture

was filtered, vacuumed and washed twice with 600 μl washing buffer. After vacuuming, the samples were immediately analyzed in a scintillation counter.

Autoradiography—Autoradiography with [^{18}F]-F0502B in human brain slices was performed similarly to previously reported methods.[75] A 48-well plate was prepared for this experiment with each well for one slice. Sections were removed from the storage buffer from −20 °C and placed into PBS + 0.1% BSA (pH 7.4) to preincubate for a while to recover to room temperature. Based on the *in vitro* binding assay, the K_d values were obtained from the binding results of the patient samples. The slices were incubated at room temperature for 30 min, rinsed in cold buffer and rinsed in distilled water once. The slices were dried and exposed to BAS TR 2025 plates (film). The films were developed after exposure for 3 h. Autoradiography images were analyzed with ImageJ (version 1.53).

Preparation of apo-α-Syn fibril and α-Syn fibril-F0502B complex—The synthesized F0502B compound was dissolved in 100% dimethyl sulfoxide (DMSO) at a concentration of 100 mM as a stock. The N-terminally acetylated wild-type (WT) human α-Syn monomer was expressed in *E. coli* BL21 (DE3) and purified as previously described.[34] To prepare apo-α-Syn fibril samples, 200 μM recombinant α-Syn monomer (in buffer containing 50 mM Tris-HCl, 150 mM KCl, 0.05% NaN_3, pH 7.5) was continuously shaken with 1% (molar ratio) preformed fibril seeds at 900 rpm in ThermoMixer (Eppendorf). The seeds were obtained by sonicating preformed α-Syn fibrils that were prepared using the same method. After 5 days of agitation, mature apo-α-Syn fibrils were used for the following cryo-EM and biochemical studies.

To prepare the α-Syn fibril-F0502B complex sample, apo-α-Syn fibrils were diluted to 3 μM and incubated with 150 μM F0502B (final DMSO concentration is 1%) for 1 h at 25 °C. An apo-α-Syn fibril sample with the same concentration of DMSO alone was prepared in parallel as a control.

Cryo-EM data collection—Four microliters of α-Syn fibril-F0502B complex or apo-α-Syn fibril was applied to the glow-discharged holey carbon Cu grids (Quantifoil R2/1, 300 mesh) twice individually and was then plunge-frozen in liquid ethane after blotted with filter paper using Vitrobot Mark IV (FEI) set at 16 °C and 95% humidity. Cryo-EM micrographs were collected using a Krios™ G4 cryo transmission electron microscope (Thermo Scientific™) operated at 300 kV with a BioContinuum™ K3 direct detector (Gatan, Inc.) in super-resolution mode. In-elastically scattered electrons were removed by a GIF Quantum energy filter (Gatan, Inc.) using a slit width of 20 eV. Forty frame movies per micrograph were recorded at ×105,000 magnification with a pixel size of 0.83 Å pixel^{-1}. The total dose was ~60 e^- Å^{-2} for a total exposure time of 2 s. For defocus values, a range of −1.6 to −2.2 μm was adopted. Automated cryo-EM data collection was performed by using EPU software (Thermo Scientific™).

Cryo-EM image pre-processing, helical reconstruction, and model building—For image pre-processing, 40 movie frames per micrograph were corrected for beam induced motion, aligned, dose-weighted, and further binned with a physical pixel size of 0.83 Å using MotionCorr2.[76] The resulting micrographs were used to estimate the contrast

transfer function using CTFFIND-4.1.8.[77] Fibrils were manually picked using the “Manual picking” program in RELION 3.1.[32]

For helical reconstruction, 120,504 manually picked fibrils from 2,567 micrographs (α-Syn fibril-F0502B complex dataset) and 29,120 manually picked fibrils from 2,868 micrographs (apo-α-Syn fibril dataset) were individually extracted to segments with a box size of 864 pixels and an inter-box distance of 71.7 Å and downscaled to 300 pixels. Then, reference-free 2D classification steps with a decreasing in-plane angular sampling rate from 8° to 0.5° and a T=2 regularization parameter were performed to calculate the apparent half pitches from the 2D class averages and discard the segments contributing suboptimal 2D class averages. An initial 3D model was constructed de novo from 2D class averages of the purified segments that comprise entire helical crossover using the relion_helix_inimodel2d program.[32] The purified segments were re-extrctedextracted using box size of 360 pixels without downscaling.

These segments and initial 3D model that was low-pass-filtered to 15 Å were further applied to perform 3D classifications (k=3) using the helical parameters calculated through the splicing of 2D class averages. The class of segments that yielded clearest 3D reconstruction map was selected and subjected to 2 additional rounds of 3D classifications (k=1) with local optimization of helical twist and rise while β-strands perpendicular to the helical axis were clearly separated. Then, 3D auto-refinements with optimization of helical twist and rise after reconstructions were carried out.

To further improve the resolution of 3D reconstruction maps, we performed contrast transfer function refinement, followed by 3D auto-refinement. Finally, the maps were sharpened with a soft-edge solvent mask using the standard “;post-processing” program in RELION 3.1.[32] Overall resolution estimates were calculated based on the gold-standard 0.143 Fourier shell correlation (FSC) between the two independently refined half-maps. For the α-Syn fibril-F0502B complex, local resolution was estimated using the Local resolution procedure in RELION 3.1 with the same mask and B-factor in post-processing.[32]

The F0502B coordinates and geometry restraints were generated using SMILES string in phenix.elbow.[62] The starting model of α-Syn was based on the structure of a recombinant α-Syn fibril (PDB ID: 6A6B).[34] The starting coordinates for both protein and ligand were then manually docked into the central region of the sharpened density map in Chimera. The three-layer protein model with two F0502B ligands was generated and manually adjusted in COOT,[61] followed by refinement against the corresponding map by phenix.real_space_refine program in PHENIX with secondary structure and geometry restraints.[62] Additional details for helical reconstruction and model building were shown in Table S4.

Radiosynthesis—The protocol for the synthesis of [^{18}F]-F0502B is as follows: all chemicals, solvents, and materials were purchased and directly used without further purification. $^{18}F^-$ was captured by a QMA light cartridge (Waters) and washed into a reactor with a mixture of Kryptofix-222 (16.67 mg/mL in CH_3CN, 0.9 mL) and K_2CO_3 (35 mg/mL in water, 0.1 mL). Then, the mixture was dried with He at 60 °C for 5 min

and then at 90 °C for another 5 min. Subsequently, 2.0 mg of compound 8b dissolved in 1.0 mL of anhydrous DMSO was added to the reactor and reacted with $^{18}F-$ at 110 °C for 15 min. Then, deprotection was performed with 1.0 ml 3 N HCl at 100 °C for 5 min. After the reaction, the mixture was neutralized with 10 ml 0.3 N $NaHCO_3$. After these steps, the mixture was loaded on a preparative HPLC (Atlantis T3 OBD 10×150 mm, 5 μm) for purification, and the column was eluted with the mobile phase at a flow rate of 4 mL/min (40:60:0.1, $CH_3CN/H_2O/CH_3COONH_3$, volume ratio). The desired fraction was collected and diluted with 20 mL of sodium ascorbate solution (0.5% m/v). Then, the diluted solution was loaded onto a C18 plus cartridge (Waters) and washed with 10 mL sodium ascorbate solution (0.5% m/v). The final radioactive product was eluted from C18 light cartridge using 1 mL absolute ethanol and was diluted with 9 mL 40% PEG for injection. A decay corrected yield of ~10% was obtained for this synthetic procedure, starting from ^{18}F-fluoride, with > 98% radiochemical and chemical purity, specific activity = 0.5-1 Ci/μmol based on radiometric HPLC and used directly for *in vitro* or *in vivo* microPET-CT imaging studies. The production was conducted away from light and the protocol for the synthesis of [^{18}F]-F0502B had a synthesis time of 100 minutes.

PET-MRI scan of rhesus macaques—Food was withheld for 12 h before scanning. After anesthesia, [^{18}F]-F0502B (111–148 MBq) was administered by a slow bolus injection through the hind limb vein. To assess the *in vivo* kinetics of [^{18}F]- F0502B in the monkey brain, a 60-minute dynamic PET scan was obtained. The results were divided by the injected dose (ID) to obtain an image region of interest-derived percentage of the ID, and the time-activity curve was then calculated. Serial 10-min static brain PET scans were acquired on a PET/CT scanner (Discovery 710, General Electric Company, Milwaukee, WI, USA) at 30, 60, and 90 min after injection. MRI was performed immediately on a 3.0T MR (750 W, General Electric Company, Milwaukee, WI, USA) after the last PET scan. T1- and T2-weighted sequences were acquired with the following parameters: TR/TE, 8.5/3.2 ms for T1 scan and 4972/113 ms for T2 scan; section thickness, 5.0 mm, gap 1.5 mm; number of slices, 20; voxel size, 0.625×0.625×5.0 mm; and field of view (FOV), 240 mm. The MR images were then imported to the AW4.6 Workstation and registered with PET images for further analysis. For DAT imaging, the monkeys were scanned with ^{11}C-CFT PET the day after [^{18}F]-F0502B PET imaging. The monkeys were injected with ^{11}C-CFT (148–185 MBq), and 10-min static brain PET scan images were obtained 60 min after ^{11}C-CFT injection.

QUANTIFICATION AND STATISTICAL ANALYSIS

Individual brain PET images were registered to a T2-weighted magnetic resonance imaging (MRI) mouse atlas (USC, Laboratory of NeuroImaging). Data are reported as the standardized update value (%ID/g x body weight). All data are expressed as mean ± SEM. from three or more independent experiments. The level of significance between the two groups was assessed with Student's *t*-test. For more than two groups, one-way ANOVA followed by LSD post hoc test was applied. A value of $P < 0.05$ was considered to be statistically significant.

Supplementary Material

Refer to Web version on PubMed Central for supplementary material.

ACKNOWLEDGMENTS

This work was supported by NIH grant (NIA RFO1, AG051538) to K.Y., the National Key Research and Development Program of China (grant no. 2019YFE0120600 to C.L. and 2019YFE0115900 to Z.Z.), the National Natural Science Foundation of China (grant no. 82271447 to Z.Z., 32170683 to D.L., and 82188101, and 32171236 to C.L.), the Science and Technology Commission of Shanghai Municipality (STCSM) (grant nos. 20XD1425000, 22JC1410400, and 2019SHZDZX02), the Shanghai Pilot Program for Basic Research – Chinese Academy of Science, Shanghai Branch (grant no. CYJ-SHFY-2022-005). We thank ADRC at Emory University for human PD, DLB, and AD patients and healthy control samples and the Cryo-Electron Microscopy Center at Interdisciplinary Research Center on Biology and Chemistry, Shanghai Institute of Organic Chemistry for help with data collection. The authors are grateful to Drs. Sydney A, Labuzan, Jessica F. Tranovich, and Melissa E. Murray from Department of Neuroscience, Mayo Clinic, Jacksonville, FL, for the human PD brain samples. The authors are grateful for the helpful discussions of Jeffrey S. Stehouwer and Chester A. Mathis from the University of Pittsburgh, and Ronald Voll and Mark M. Goodman from Emory University School of Medicine. The human brain Ki assays were performed by Chester A. Mathis at the University of Pittsburgh.

INCLUSION AND DIVERSITY

We support inclusive, diverse, and equitable conduct of research.

REFERENCES

1. Dev KK, Hofele K, Barbieri S, Buchman VL, and van der Putten H (2003). Part II: alpha-synuclein and its molecular pathophysiological role in neurodegenerative disease. Neuropharmacology 45, 14–44. [PubMed: 12814657]
2. Theillet FX, Binolfi A, Bekei B, Martorana A, Rose HM, Stuiver M, Verzini S, Lorenz D, van Rossum M, Goldfarb D, and Selenko P (2016). Structural disorder of monomeric alpha-synuclein persists in mammalian cells. Nature 530, 45–50. 10.1038/nature16531. [PubMed: 26808899]
3. Olanow CW, and Brundin P (2013). Parkinson's disease and alpha synuclein: is Parkinson's disease a prion-like disorder? Mov. Disord 28, 31–40. 10.1002/mds.25373. [PubMed: 23390095]
4. Jucker M, and Walker LC (2013). Self-propagation of pathogenic protein aggregates in neurodegenerative diseases. Nature 501, 45–51. 10.1038/nature12481. [PubMed: 24005412]
5. Shahnawaz M, Mukherjee A, Pritzkow S, Mendez N, Rabadia P, Liu X, Hu B, Schmeichel A, Singer W, Wu G, et al. (2020). Discriminating alpha-synuclein strains in Parkinson's disease and multiple system atrophy. Nature 578, 273–277. 10.1038/s41586-020-1984-7. [PubMed: 32025029]
6. Peelaerts W, Bousset L, Van der Perren A, Moskalyuk A, Pulizzi R, Giugliano M, Van den Haute C, Melki R, and Baekelandt V (2015). Alpha-synuclein strains cause distinct synucleinopathies after local and systemic administration. Nature 522, 340–344. 10.1038/nature14547. [PubMed: 26061766]
7. Volpicelli-Daley L, and Brundin P (2018). Prion-like propagation of pathology in Parkinson disease. Handb. Clin. Neurol 153, 321–335. 10.1016/B978-0-444-63945-5.00017-9. [PubMed: 29887143]
8. Galpern WR, and Lang AE (2006). Interface between tauopathies and synucleinopathies: a tale of two proteins. Ann. Neurol 59, 449–458. 10.1002/ana.20819. [PubMed: 16489609]
9. Gomperts SN, Locascio JJ, Makaretz SJ, Schultz A, Caso C, Vasdev N, Sperling R, Growdon JH, Dickerson BC, and Johnson K (2016). Tau positron emission tomographic imaging in the Lewy body diseases. JAMA Neurol. 73, 1334–1341. 10.1001/jamaneurol.2016.3338. [PubMed: 27654968]
10. Schumacher J, Gunter JL, Przybelski SA, Jones DT, Graff-Radford J, Savica R, Schwarz CG, Senjem ML, Jack CR, Lowe VJ, et al. (2021). Dementia with Lewy bodies: association of Alzheimer pathology with functional connectivity networks. Brain 144, 3212–3225. 10.1093/brain/awab218. [PubMed: 34114602]

11. Uéda K, Fukushima H, Masliah E, Xia Y, Iwai A, Yoshimoto M, Otero DA, Kondo J, Ihara Y, and Saitoh T (1993). Molecular cloning of cDNA encoding an unrecognized component of amyloid in Alzheimer disease. Proc. Natl. Acad. Sci. USA 90, 11282–11286. [PubMed: 8248242]
12. Masliah E, Rockenstein E, Veinbergs I, Sagara Y, Mallory M, Hashimoto M, and Mucke L (2001). Beta-amyloid peptides enhance alpha-synuclein accumulation and neuronal deficits in a transgenic mouse model linking Alzheimer's disease and Parkinson's disease. Proc. Natl. Acad. Sci. USA 98, 12245–12250. 10.1073/pnas.211412398. [PubMed: 11572944]
13. Wakisaka Y, Furuta A, Tanizaki Y, Kiyohara Y, Iida M, and Iwaki T (2003). Age-associated prevalence and risk factors of Lewy body pathology in a general population: the Hisayama study. Acta Neuropathol. 106, 374–382. 10.1007/s00401-003-0750-x. [PubMed: 12904992]
14. Kurata T, Kawarabayashi T, Murakami T, Miyazaki K, Morimoto N, Ohta Y, Takehisa Y, Nagai M, Ikeda M, Matsubara E, Westaway D, Hyslop PS, Harigaya Y, Kamiya T, Shoji M, and Abe K (2007). Enhanced accumulation of phosphorylated alpha-synuclein in double transgenic mice expressing mutant beta-amyloid precursor protein and presenilin-1 [J]. J Neurosci Res 85 (10), 2246–2252. [PubMed: 17526016]
15. Goedert M, Clavaguera F, and Tolnay M (2010). The propagation of prion-like protein inclusions in neurodegenerative diseases. Trends Neurosci. 33, 317–325. 10.1016/j.tins.2010.04.003. [PubMed: 20493564]
16. Harada R, Okamura N, Furumoto S, and Yanai K (2018). Imaging protein misfolding in the brain using beta-sheet ligands. Front. Neurosci 12, 585. 10.3389/fnins.2018.00585. [PubMed: 30186106]
17. Jovalekic A, Koglin N, Mueller A, and Stephens AW (2017). New protein deposition tracers in the pipeline. EJNMMI Radiopharm. Chem 1, 11. 10.1186/s41181-016-0015-3. [PubMed: 29564387]
18. Raval NR, Madsen CA, Shalgunov V, Nasser A, Battisti UM, Beaman EE, Juhl M, Jørgensen LM, Herth MM, Hansen HD, et al. (2022). Evaluation of the alpha-synuclein PET radiotracer (d(3))-[(11)C] MODAG-001 in pigs. Nucl. Med. Biol 114–115, 42–48. 10.1016/j.nucmedbio.2022.08.001.
19. Chen MK, Kuwabara H, Zhou Y, Adams RJ, Brasić JR, McGlothan JL, Verina T, Burton NC, Alexander M, Kumar A, et al. (2008). VMAT2 and dopamine neuron loss in a primate model of Parkinson's disease. J. Neurochem 105, 78–90. 10.1111/j.1471-4159.2007.05108.x. [PubMed: 17988241]
20. Ishiwata K, Kimura Y, Oda K, Ishii K, Sakata M, Kawasaki K, Nariai T, Suzuki Y, Ishibashi K, Mishina M, et al. (2010). Development of PET radiopharmaceuticals and their clinical applications at the Positron Medical Center. Geriatr. Gerontol. Int 10, S180–S196. 10.1111/j.1447-0594.2010.00594.x. [PubMed: 20590833]
21. de la Fuente-Fernández R. (2012). Role of DaTSCAN and clinical diagnosis in Parkinson disease. Neurology 78, 696–701. 10.1212/WNL.0b013e318248e520. [PubMed: 22323748]
22. Perlmutter JS, and Eidelberg D (2012). To scan or not to scan: DaT is the question. Neurology 78, 688–689. 10.1212/WNL.0b013e3182494c72. [PubMed: 22323757]
23. Winogrodzka A, Wagenaar RC, Booij J, and Wolters EC (2005). Rigidity and bradykinesia reduce interlimb coordination in Parkinsonian gait [J]. Arch Phys Med Rehabil 86, 183–189. [PubMed: 15706541]
24. Zhang Z, Kang SS, Liu X, Ahn EH, Zhang Z, He L, Iuvone PM, Duong DM, Seyfried NT, Benskey MJ, et al. (2017). Asparagine endopeptidase cleaves alpha-synuclein and mediates pathologic activities in Parkinson's disease. Nat. Struct. Mol. Biol 24, 632–642. 10.1038/nsmb.3433. [PubMed: 28671665]
25. Conway KA, Rochet JC, Bieganski RM, and Lansbury PT Jr. (2001). Kinetic stabilization of the alpha-synuclein protofibril by a dopamine-alpha-synuclein adduct. Science 294, 1346–1349. 10.1126/science.1063522. [PubMed: 11701929]
26. Hu Q, Uversky VN, Huang M, Kang H, Xu F, Liu X, Lian L, Liang Q, Jiang H, Liu A, et al. (2016). Baicalein inhibits alpha-synuclein oligomer formation and prevents progression of alpha-synuclein accumulation in a rotenone mouse model of Parkinson'sdisease. Biochim. Biophys. Acta 1862, 1883–1890. 10.1016/j.bbadis.2016.07.008. [PubMed: 27425033]

27. Hung KC, Huang HJ, Wang YT, and Lin AM (2016). Baicalein attenuates alpha-synuclein aggregation, inflammasome activation and autophagy in the MPP(+)-treated nigrostriatal dopaminergic system in vivo. J. Ethnopharmacol 194, 522–529. 10.1016/j.jep.2016.10.040. [PubMed: 27742410]

28. Zhang X, Jin H, Padakanti PK, Li J, Yang H, Fan J, Mach RH, Kotzbauer P, and Tu Z (2014). Radiosynthesis and in vivo evaluation of two PET radioligands for imaging alpha-synuclein. Appl. Sci. (Basel) 4, 66–78. 10.3390/app4010066. [PubMed: 25642331]

29. Wagner J, Ryazanov S, Leonov A, Levin J, Shi S, Schmidt F, Prix C, Pan-Montojo F, Bertsch U, Mitteregger-Kretzschmar G, et al. (2013). Anle138b: a novel oligomer modulator for disease-modifying therapy of neurodegenerative diseases such as prion and Parkinson's disease. Acta Neuropathol. 125, 795–813. 10.1007/s00401-013-1114-9. [PubMed: 23604588]

30. Volpicelli-Daley LA, Gamble KL, Schultheiss CE, Riddle DM, West AB, and Lee VM (2014). Formation of alpha-synuclein Lewy neurite-like aggregates in axons impedes the transport of distinct endosomes. Mol. Biol. Cell 25, 4010–4023. 10.1091/mbc.E14-02-0741. [PubMed: 25298402]

31. Fodero-Tavoletti MT, Mulligan RS, Okamura N, Furumoto S, Rowe CC, Kudo Y, Masters CL, Cappai R, Yanai K, and Villemagne VL (2009). In vitro characterisation of BF227 binding to alpha-synuclein/Lewy bodies. Eur. J. Pharmacol 617, 54–58. 10.1016/j.ejphar.2009.06.042. [PubMed: 19576880]

32. Scheres SHW (2020). Amyloid structure determination in RELION-3.1. Acta Crystallogr. Sect.: Struct. Biol 76, 94–101.

33. Guerrero-Ferreira R, Taylor NM, Arteni AA, Kumari P, Mona D, Ringler P, Britschgi M, Lauer ME, Makky A, Verasdonck J, et al. (2019). Two new polymorphic structures of human full-length alpha-synuclein fibrils solved by cryo-electron microscopy. eLife 8, e48907. 10.7554/eLife.48907. [PubMed: 31815671]

34. Li Y, Zhao C, Luo F, Liu Z, Gui X, Luo Z, Zhang X, Li D, Liu C, and Li X (2018). Amyloid fibril structure of α-synuclein determined by cryo-electron microscopy. Cell Res. 28, 897–903. [PubMed: 30065316]

35. Zhao Y, Li J, Gu H, Wei D, Xu Y-C, Fu W, and Yu Z (2015). Conformational preferences of π–π stacking between ligand and protein, analysis derived from crystal structure data geometric preference of π–π interaction. Interdiscip. Sci. Comp. Life Sci 7, 211–220.

36. Šukalović V, Zlatović M, Roglić G, Kostić Rajačić S, and Andrić D (2009). Application of hybrid density functional theory in calculation of edge-to-face interactions of receptor-ligand system. Acta Chim. Slov 56, 270–277.

37. Lucas X, Bauzá A, Frontera A, and Quiñonero D (2016). A thorough anion–π interaction study in biomolecules: on the importance of cooperativity effects. Chem. Sci 7, 1038–1050. [PubMed: 29899893]

38. Auffinger P, Hays FA, Westhof E, and Ho PS (2004). Halogen bonds in biological molecules. Proc. Natl. Acad. Sci. USA 101, 16789–16794. [PubMed: 15557000]

39. Sun Y, Hou S, Zhao K, Long H, Liu Z, Gao J, Zhang Y, Su X-D, Li D, and Liu C (2020). Cryo-EM structure of full-length α-synuclein amyloid fibril with Parkinson's disease familial A53T mutation. Cell Res. 30, 360–362. [PubMed: 32203130]

40. Schweighauser M, Shi Y, Tarutani A, Kametani F, Murzin AG, Ghetti B, Matsubara T, Tomita T, Ando T, and Hasegawa K (2020). Structures of α-synuclein filaments from multiple system atrophy. Nature 585, 464–469. [PubMed: 32461689]

41. Shimozawa A, Ono M, Takahara D, Tarutani A, Imura S, Masuda-Suzukake M, Higuchi M, Yanai K, Hisanaga SI, and Hasegawa M (2017). Propagation of pathological α-synuclein in marmoset brain. Acta Neuropathol. Commun 5, 12. 10.1186/s40478-017-0413-0. [PubMed: 28148299]

42. Eslamboli A, Romero-Ramos M, Burger C, Bjorklund T, Muzyczka N, Mandel RJ, Baker H, Ridley RM, and Kirik D (2007). Long-term consequences of human alpha-synuclein overexpression in the primate ventral midbrain. Brain 130, 799–815. 10.1093/brain/awl382. [PubMed: 17303591]

43. Villemagne VL, Okamura N, Pejoska S, Drago J, Mulligan RS, Chételat G, O'Keefe G, Jones G, Kung HF, Pontecorvo M, et al. (2012). Differential diagnosis in Alzheimer's disease and

dementia with Lewy bodies via VMAT2 and amyloid imaging. Neurodegener. Dis 10, 161–165. 10.1159/000334535. [PubMed: 22261520]

44. Okamura N, Furumoto S, Fodero-Tavoletti MT, Mulligan RS, Harada R, Yates P, Pejoska S, Kudo Y, Masters CL, Yanai K, et al. (2014). Non-invasive assessment of Alzheimer's disease neurofibrillary pathology using 18F-THK5105 PET. Brain 137, 1762–1771. 10.1093/brain/awu064. [PubMed: 24681664]
45. Kikuchi T, Okamura T, Zhang MR, Fukushi K, and Irie T (2010). In vivo evaluation of N-[18F]fluoroethylpiperidin-4ylmethyl acetate in rats compared with MP4A as a probe for measuring cerebral acetylcholinesterase activity. Synapse 64, 209–215. 10.1002/syn.20720. [PubMed: 19862687]
46. Yu L, Cui J, Padakanti PK, Engel L, Bagchi DP, Kotzbauer PT, and Tu Z (2012). Synthesis and in vitro evaluation of alpha-synuclein ligands. Bioorg. Med. Chem 20, 4625–4634. 10.1016/j.bmc.2012.06.023. [PubMed: 22789706]
47. Chu W, Zhou D, Gaba V, Liu J, Li S, Peng X, Xu J, Dhavale D, Bagchi DP, d'Avignon A, et al. (2015). Design, synthesis, and characterization of 3-(benzylidene)indolin-2-one derivatives as ligands for alpha-synuclein fibrils. J. Med. Chem 58, 6002–6017. 10.1021/acs.jmedchem.5b00571. [PubMed: 26177091]
48. Zhu M, Rajamani S, Kaylor J, Han S, Zhou F, and Fink AL (2004). The flavonoid baicalein inhibits fibrillation of alpha-synuclein and disaggregates existing fibrils. J. Biol. Chem 279, 26846–26857. 10.1074/jbc.M403129200. [PubMed: 15096521]
49. Meng X, Munishkina LA, Fink AL, and Uversky VN (2009). Molecular mechanisms underlying the flavonoid-induced inhibition of alpha-synuclein fibrillation. Biochemistry 48, 8206–8224. 10.1021/bi900506b. [PubMed: 19634918]
50. Schütz AK, Soragni A, Hornemann S, Aguzzi A, Ernst M, Böckmann A, and Meier BH (2011). The amyloid–Congo red interface at atomic resolution. Angew. Chem. Int. Ed. Engl 50, 5956–5960. [PubMed: 21591034]
51. Landau M, Sawaya MR, Faull KF, Laganowsky A, Jiang L, Sievers SA, Liu J, Barrio JR, and Eisenberg D (2011). Towards a pharmacophore for amyloid. PLoS Biol. 9, e1001080. [PubMed: 21695112]
52. Wolfe LS, Calabrese MF, Nath A, Blaho DV, Miranker AD, and Xiong Y (2010). Protein-induced photophysical changes to the amyloid indicator dye Thioflavin T. Proc. Natl. Acad. Sci. USA 107, 16863–16868. [PubMed: 20826442]
53. Childers WS, Mehta AK, Lu K, and Lynn DG (2009). Templating molecular arrays in amyloid's cross-β grooves. J. Am. Chem. Soc 131, 10165–10172. [PubMed: 19569651]
54. Krebs MR, Bromley EH, and Donald AM (2005). The binding of thioflavin-T to amyloid fibrils: localisation and implications. J. Struct. Biol 149, 30–37. [PubMed: 15629655]
55. Shi Y, Murzin AG, Falcon B, Epstein A, Machin J, Tempest P, Newell KL, Vidal R, Garringer HJ, and Sahara N (2021). Cryo-EM structures of tau filaments from Alzheimer's disease with PET ligand APN-1607. Acta Neuropathol. 141, 697–708. [PubMed: 33723967]
56. Ferrie JJ, Lengyel-Zhand Z, Janssen B, Lougee MG, Giannakoulias S, Hsieh C-J, Pagar VV, Weng C-C, Xu H, and Graham TJ (2020). Identification of a nanomolar affinity α-synuclein fibril imaging probe by ultra-high throughput in silico screening. Chem. Sci 11, 12746–12754. [PubMed: 33889379]
57. Jiang L, Liu C, Leibly D, Landau M, Zhao M, Hughes MP, and Eisenberg DS (2013). Structure-based discovery of fiber-binding compounds that reduce the cytotoxicity of amyloid beta. eLife 2, e00857. [PubMed: 23878726]
58. Korat Š, Bidesi NSR, Bonanno F, Di Nanni A, Hoàng ANN, Herfert K, Maurer A, Battisti UM, Bowden GD, and Thonon D (2021). Alpha-synuclein PET tracer development—an overview about current efforts. Pharmaceuticals (Basel) 14, 847. [PubMed: 34577548]
59. Yang Y, Shi Y, Schweighauser M, Zhang X, Kotecha A, Murzin AG, Garringer HJ, Cullinane PW, Saito Y, Foroud T, et al. (2022). Structures of alpha-synuclein filaments from human brains with Lewy pathology [J]. Nature 610, 791–795.
60. Schneider CA, Rasband WS, and Eliceiri KW (2012). NIH Image to ImageJ: 25 years of image analysis. Nat. Methods 9, 671–675. 10.1038/nmeth.2089. [PubMed: 22930834]

61. Emsley P, Lohkamp B, Scott WG, and Cowtan K (2010). Features and development of coot. Acta Crystallogr. D Biol. Crystallogr 66, 486–501. 10.1107/S0907444910007493. [PubMed: 20383002]
62. Adams PD, Afonine PV, Bunkóczi G, Chen VB, Davis IW, Echols N, Headd JJ, Hung LW, Kapral GJ, Grosse-Kunstleve RW, et al. (2010). Phenix: a comprehensive Python-based system for macromolecular structure solution. Acta Crystallogr. D Biol. Crystallogr 66, 213–221. 10.1107/S0907444909052925. [PubMed: 20124702]
63. Qiu L, Jiang H, Yu Y, Gu J, Wang J, Zhao H, Huang T, Gropler RJ, Klein RS, Perlmutter JS, and Tu Z (2022). Radiosynthesis and evaluation of a fluorine-18 radiotracer [(18)F]FS1P1 for imaging sphingo-sine-1-phosphate receptor 1. Org. Biomol. Chem 20, 1041–1052. 10.1039/d1ob02225c. [PubMed: 35029272]
64. Bindoli S, Galozzi P, Magnani F, Rubin L, Campi C, Doria A, Cecchin D, and Sfriso P (2020). F-Fluorodeoxyglucose positron emission tomography and computed tomography with magnetic resonance for diagnosing adult-onset Still's disease. Front. Med. (Lausanne) 18, 544412. 10.3389/fmed.2020.544412.
65. Wang ZH, Liu P, Liu X, Yu SP, Wang JZ, and Ye K (2018). Delta-secretase (AEP) mediates tau-splicing imbalance and accelerates cognitive decline in tauopathies. J. Exp. Med 215, 3038–3056. 10.1084/jem.20180539. [PubMed: 30373880]
66. Ahn EH, Kang SS, Liu X, Chen G, Zhang Z, Chandrasekharan B, Alam AM, Neish AS, Cao X, and Ye K (2020). Initiation of Parkinson's disease from gut to brain by delta-secretase. Cell Res. 30, 70–87. 10.1038/s41422-019-0241-9. [PubMed: 31649329]
67. Miller DL, Papayannopoulos IA, Styles J, Bobin SA, Lin YY, Biemann K, and Iqbal K (1993). Peptide compositions of the cerebrovascular and senile plaque core amyloid deposits of Alzheimer's disease. Arch. Biochem. Biophys 301, 41–52. 10.1006/abbi.1993.1112. [PubMed: 8442665]
68. Fitzpatrick AWP, Falcon B, He S, Murzin AG, Murshudov G, Garringer HJ, Crowther RA, Ghetti B, Goedert M, and Scheres SHW (2017). Cryo-EM structures oftau filaments from Alzheimer's disease. Nature 547, 185–190. 10.1038/nature23002. [PubMed: 28678775]
69. Goedert M, Spillantini MG, Cairns NJ, and Crowther RA (1992). Tau proteins of Alzheimer paired helical filaments: abnormal phosphorylation of all six brain isoforms. Neuron 8, 159–168. 10.1016/0896-6273(92)90117-v. [PubMed: 1530909]
70. Iqbal K, Zaidi T, Thompson CH, Merz PA, and Wisniewski HM (1984). Alzheimer paired helical filaments: bulk isolation, solubility, and protein composition. Acta Neuropathol. 62, 167–177. 10.1007/BF00691849. [PubMed: 6538056]
71. Peng C, Gathagan RJ, Covell DJ, Medellin C, Stieber A, Robinson JL, Zhang B, Pitkin RM, Olufemi MF, Luk KC, et al. (2018). Cellular milieu imparts distinct pathological alpha-synuclein strains in alpha-synucleinopathies. Nature 557, 558–563. 10.1038/s41586-018-0104-4. [PubMed: 29743672]
72. Sheldrick GM (2015). Crystal structure refinement with SHELXL. Acta Crystallogr. C Struct. Chem 71, 3–8. 10.1107/S2053229614024218. [PubMed: 25567568]
73. Dolomanov OV, Bourhis LJ, Gildea RJ, Howard JAK, and Puschmann H (2009). OLEX2: A complete structure solution, refinement and analysis program. J. Appl. Crystallogr 42, 339–341. 10.1107/S0021889808042726.
74. Klunk WE, Wang Y, Huang GF, Debnath ML, Holt DP, Shao L, Hamilton RL, Ikonomovic MD, DeKosky ST, and Mathis CA (2003). The binding of 2-(4′-methylaminophenyl)benzothiazole to post-mortem brain homogenates is dominated by the amyloid component. J. Neurosci 23, 2086–2092. [PubMed: 12657667]
75. Hostetler ED, Walji AM, Zeng Z, Miller P, Bennacef I, Salinas C, Connolly B, Gantert L, Haley H, Holahan M, et al. (2016). Preclinical characterization of 18F-MK-6240, a promising PET tracer for in vivo quantification of human neurofibrillary tangles. J. Nucl. Med 57, 1599–1606. 10.2967/jnumed.115.171678. [PubMed: 27230925]
76. Zheng SQ, Palovcak E, Armache J-P, Verba KA, Cheng Y, and Agard DA (2017). MotionCor2: anisotropic correction of beam-induced motion for improved cryo-electron microscopy. Nat. Methods 14, 331–332. [PubMed: 28250466]

77. Rohou A, and Grigorieff N (2015). CTFFIND4: fast and accurate defocus estimation from electron micrographs. J. Struct. Biol 192, 216–221. [PubMed: 26278980]

Highlights

- The F0502B PET tracer binds with high affinity to α-synuclein but not to Aβ and Tau
- F0502B recognizes α-synuclein aggregates in mouse, macaque, and PD human brains
- Cryo-EM structure of the α-synuclein fibril-F0502B complex reveals binding insights
- Promising lead compound for imaging α-synuclein inclusions in synucleinopathies

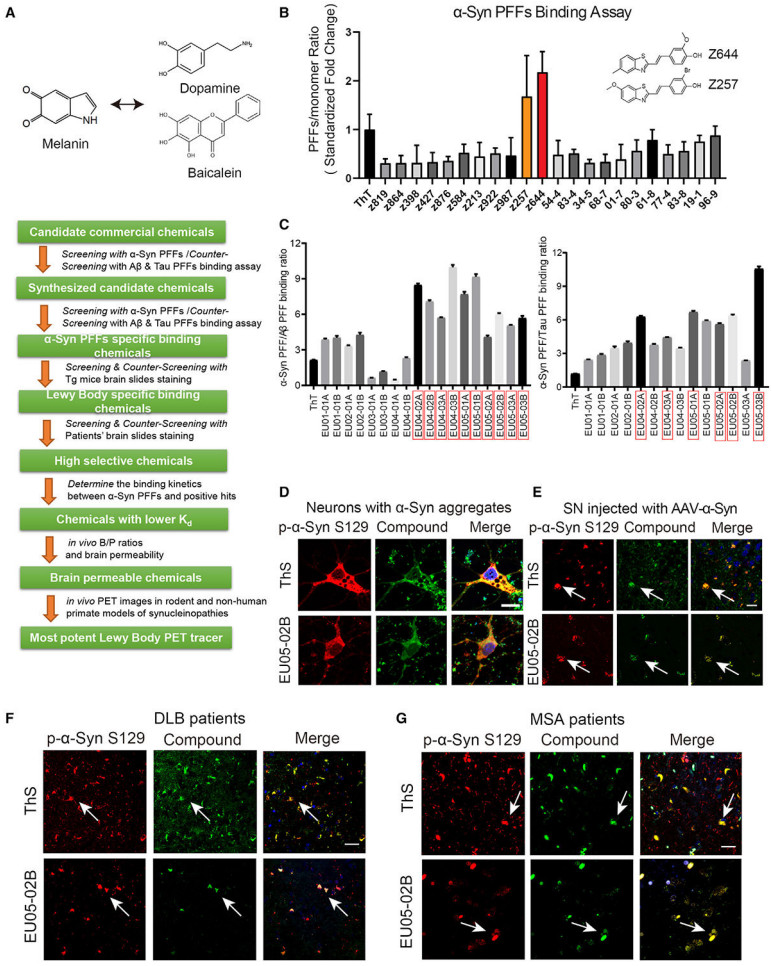

Figure 1. Drug design strategy and screening of potential imaging agents for synucleinopathies

For a Figure360 author presentation of Figure 1, see https://doi.org/10.1016/j.cell.2023.06.004

(A) The screening strategy of α-Syn PET tracers.

(B) Screening candidate chemicals using spectrophotometric assay with α-Syn PFFs. The emission wavelength was determined based on the excitation wavelength of each chemical. The PFF/monomer binding ratio was standardized by the ThT binding fold change. Error bars represent the mean ± SEM. Data are representative of 7 independent experiments.

(C) The second round of screening of candidate chemicals with the α-Syn PFF versus Aβ/Tau PFF binding ratios. Error bars represent the mean ± SEM. Data are representative of 5 independent experiments.

(D) Confocal fluorescence images of neurons containing α-Syn aggregates. The neurons were infected with AAV-α-Syn at days *in vitro* (DIV) 7 and transduced with α-Syn PFFs at DIV 12. The samples were immunostained with anti-p-α-Syn S129 (pseudocolors were converted to red) together with ThT or EU05-02B (0.1 μM). Scale bars, 10 μm.

(E) Double staining of α-Syn aggregates in AAV-α-Syn A53T-injected mouse SN with pS129 antibody and EU05-02B or ThS. EU05-02B sensitively captured α-Syn aggregates in the SN (arrows). Scale bars, 20 μm.

(F) Double staining of α-Syn aggregates in the cortex of DLB patients with pS129 antibody and EU05-02B or ThS. Scale bars, 20 μm.
(G) Double staining of α-Syn aggregates in the SN of MSA patients with pS129 antibody and EU05-02B or ThS. Scale bars, 20 μm.
See also Figures S1 and S2.

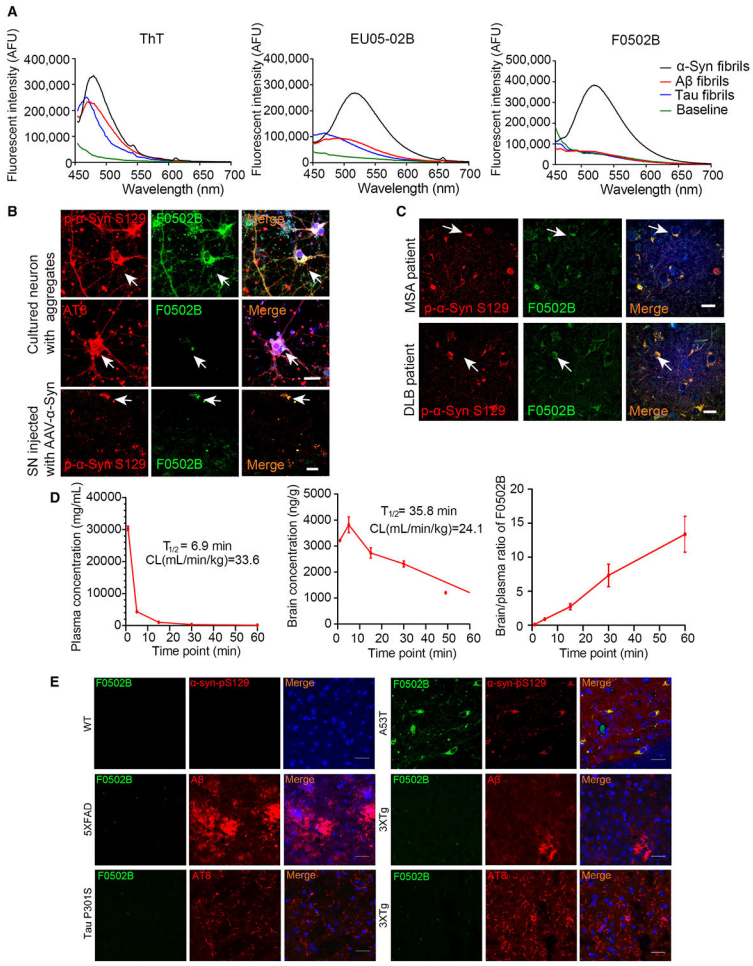

Figure 2. F0502B selectively binds to α-Syn aggregates *in vitro* and *ex vivo*

(A) The binding of ThT, EU05-02B, and F0502B to α-Syn, Aβ, and Tau PFFs. ThT binding with the same PFF concentration showed a binding peak at 485 nm. EU05-02B and F0502B showed stronger binding affinity with α-Syn PFFs than with Aβ and Tau PFFs.

(B and C) Characterization of EU05-02B selectivity for aggregates in cultured neurons, mouse SN region expressing α-Syn A53T, and brain slices from DLB (cortex) and MSA (SN) patients (arrows show co-localization signals). Scale bars, 20 μm.

(D) The levels of F0502B in the plasma and brain homogenates of male ICR mice that received i.v. injection of 5 mg/kg F0502B. The B/P ratio was determined at different time points. Error bars represent the mean ± SD. Data are representative of 3 mice at every time point.

(E) Staining of inclusions in WT, 5xFAD, Tau P301S, 3xTg (cortex), and AAV-α-Syn A53T-injected mice (SN) intravenously administered F0502B (2 mg/kg). The tissues were prepared at 2 h after tracer administration. Scale bars, 20 μm.

See also Figures S3 and S4.

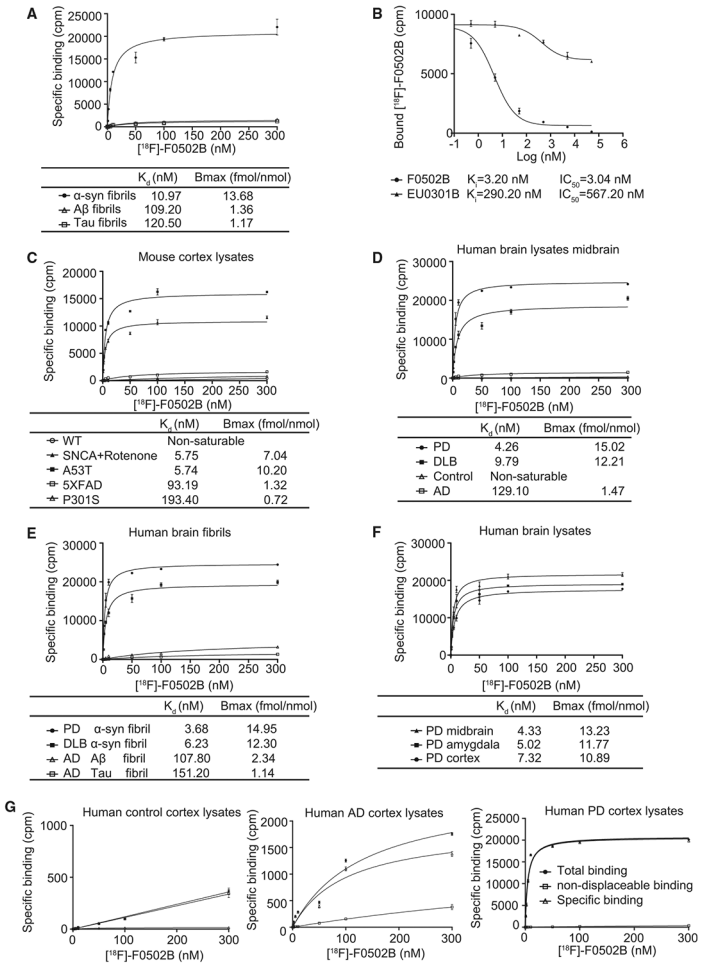

Figure 3. [^{18}F]-F0502B binding affinity and selectivity to different protein aggregates *in vitro*

(A) Quantification of binding affinities. The binding affinities of [^{18}F]-F0502B to α-Syn, Aβ, or Tau PFFs were determined in saturation binding studies. Data points represent the mean ± SD. Similar results were obtained in more than three independent experiments.

(B) [^{18}F]-F0502B competitive binding assays with α-Syn PFFs. Data points represent the mean ± SD.

(C) F0502B saturation binding assays with unfractionated AD/PD/control mouse brain homogenates. The α-Syn aggregates in SNCA transgenic mice treated with rotenone or AAV-α-Syn A53T-injected mice displayed strong binding activities with a K_d of 5.75 nM. Data points represent the mean ± SD.

(D and E) F0502B saturation binding assays with unfractionated human PD/DLB/AD/control brain homogenates and insoluble protein fractions from human PD/DLB/AD/brain samples. Both PD and DLB brain homogenates and insoluble fractions exhibited robust binding activities with K_d values of 4.26/9.79 and 3.68/6.23 nM, respectively. Data points represent the mean ± SD.

(F) F0502B saturation binding assays of unfractionated human PD brain homogenates from different brain areas. B_{max} (fmol/nmol) = CPM/(2.22 * 10^{12} dpm/Ci * 0.75 cpm/dpm *2,000 Ci/mmol *10^{-12} mmol/fmol *0.5 nmol). All of the brain regions, including the midbrain, amygdala, and cortex, displayed prominent binding activities. Midbrain homogenates show

the strongest binding. Error bars represent the mean ± SD. Data are representative of 3 independent experiments.

(G) Total, specific, and non-displaceable binding (NDB) from saturation binding studies with [^{18}F]-F0502B in the frontal cortex of healthy control, AD, and PD patients. NDB was defined by self-block at 100 × K_d concentration. Error bars represent the mean ± SD. Data are representative of 3 independent experiments.

See also Figure S3F.

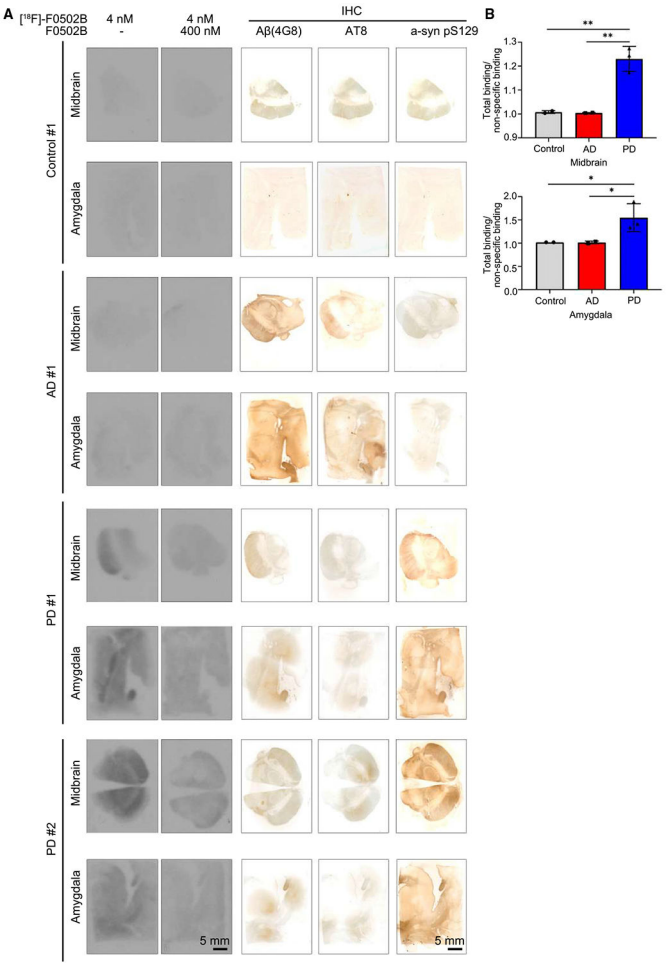

Figure 4. [^{18}F]-F0502B binding affinity and selectivity to different human brain slides

(A) Autoradiographic labeling of adjacent brain sections from patients with [^{18}F]-F0502B (4 nM). Total binding of [^{18}F]-F0502B was markedly abolished by the addition of non-radioactive F0502B (400 nM), except for the nonspecific (NS) labeling of white matter (left 2 lanes). Scale bars, 5 mm. The serial sections of each group were immunostained with antibodies against Aβ, p-Tau, and pS129 α-Syn (right 3 lanes). PD patient brains displayed specific [^{18}F]-F0502B signals coupled with demonstrable pS129 staining. Scale bars, 5 mm. (B) Quantification of [^{18}F]-F0502B binding in human brain slices. The total mean signal intensity for specific brain regions was normalized to the nonspecific signal intensity of the same region. Error bars represent the mean ± SEM. Statistical significance was determined using a two-way ANOVA followed by post hoc Bonferroni test for multiple group comparison. Data represent three independent experiments using 3 controls, 3 AD patients, and 3 PD patients in the midbrain and amygdala. *$p < 0.05$, **$p < 0.01$.

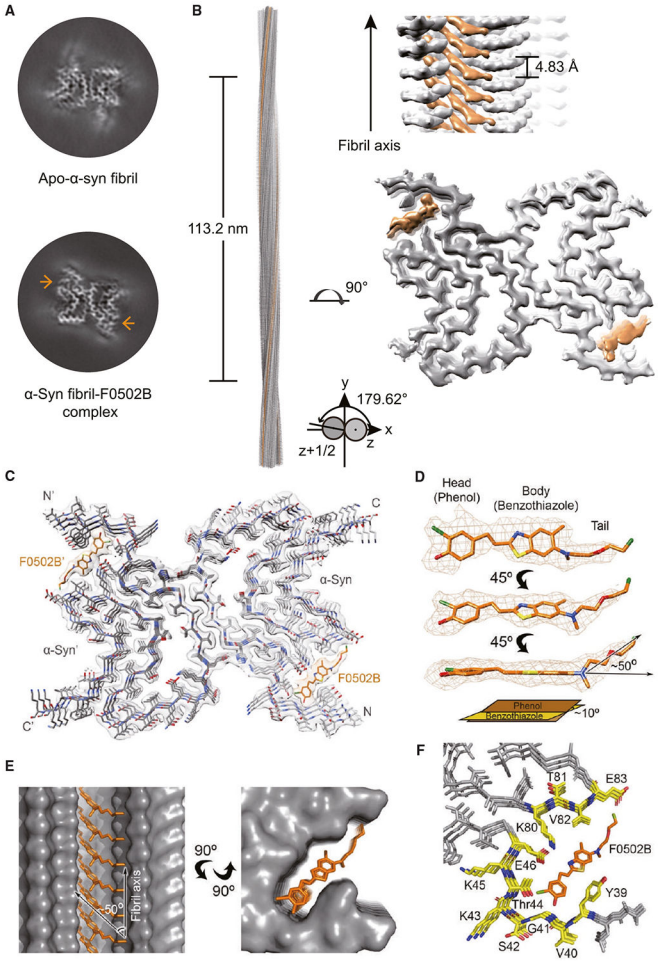

Figure 5. Cryo-EM structure of the α-Syn fibril-F0502B complex

(A) Central slices of the 3D maps of the apo-α-Syn fibril (top) and α-Syn fibril-F0502B complex (bottom). The additional densities are indicated by arrows.

(B) Cryo-EM 3D reconstruction density map of the α-Syn fibril-F0502B complex. Fibril parameters including the length of half pitch (180° helical turn), twist angle, and helical rise are indicated. Extra densities are colored in orange.

(C) Cross-section view of the structural model of the α-Syn fibril-F0502B complex fitted in the density map. α-Syn is colored in gray. Ligand F0502B is colored in orange.

(D) Enlarged view of the F0502B structural model superimposed with the ligand density (mesh). The dihedral angle between the phenol and benzothiazole-ethenyl planes is ~10°. The angle between the fluoro tail and the benzothiazole-ethenyl plane is ~50°.

(E) Views of F0502B molecules stacking in the ligand-binding tunnel along the fibril axis (side view, left; top view, right). The surface of α-Syn fibril is shown and colored in gray. F0502B is shown in sticks and colored in orange. The angle between the F0502B body plane and fibril axis is ~50°.

(F) Enlarged top view of the F0502B binding cavity with the surrounding residues shown in sticks and highlighted in yellow.

See also Figure S5.

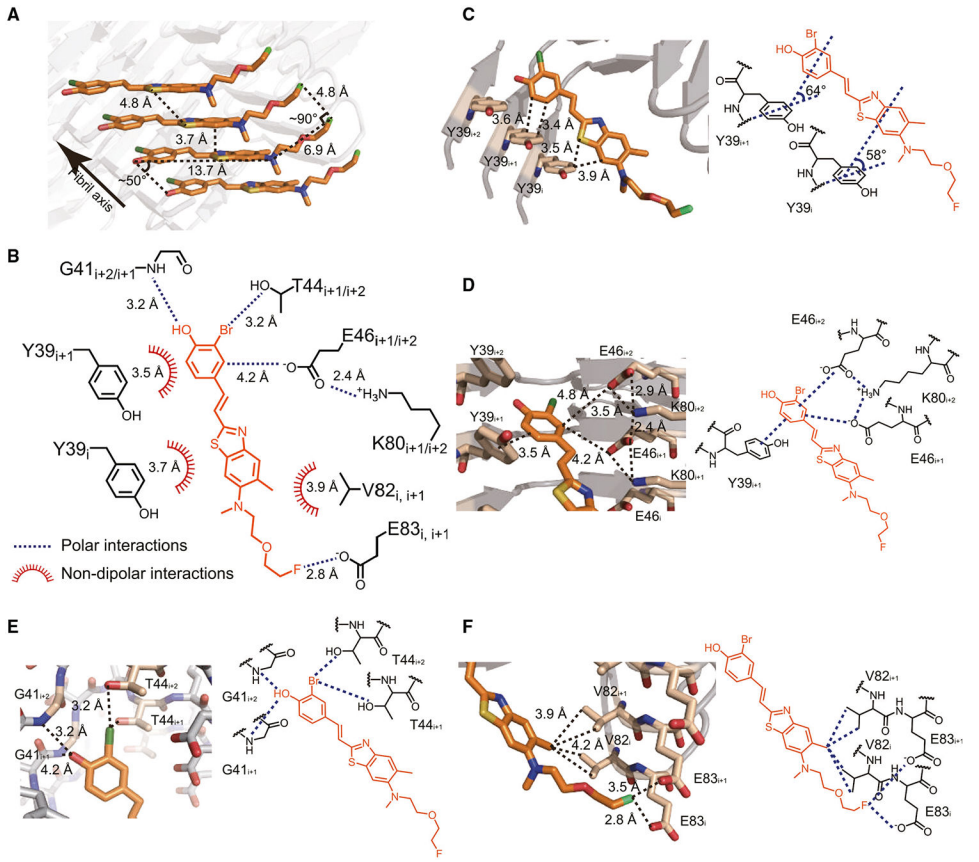

Figure 6. Interactions between F0502B and α-Syn fibril

(A) π-π stacking among F0502B molecules. The distance between neighboring aromatic rings of F0502B is ~3.7 Å. Detailed interaction distances are labeled.

(B) Summary of the molecular interactions between F0502B (orange) and α-Syn fibril (black). Polar interactions (blue dashed lines) and non-dipolar interactions (red spiked arcs) are depicted with interaction distances.

(C) T-shaped π-π interactions between F0502B and Tyr39 residues in three consecutive α-Syn molecules (i, i+1, i+2) along the fibril. Detailed interaction distances and the dihedral angles formed by π planes are labeled.

(D) Cation-anion-π-π network between the phenol head of F0502B and α-Syn residues Lys80, Glu46, and Tyr39. Detailed interaction distances are labeled.

(E) Hydrogen bonding and halogen bonding interactions between the phenol head of F0502B and α-Syn. The phenolic hydroxyl group of F0502B forms hydrogen bonds with the backbone amide of Gly41. The bromine of F0502B interacts with the sidechain hydroxyl group of Thr44 via halogen bonding. Detailed interaction distances are labeled.

(F) Hydrophobic and halogen bonding interactions between the tail of F0502B and α-Syn. The methyl group of F0502B forms hydrophobic interactions with Val82. The fluorine of F0502B forms halogen bonding interactions with Glu83. Detailed interaction distances are labeled.

See also Figure S6.

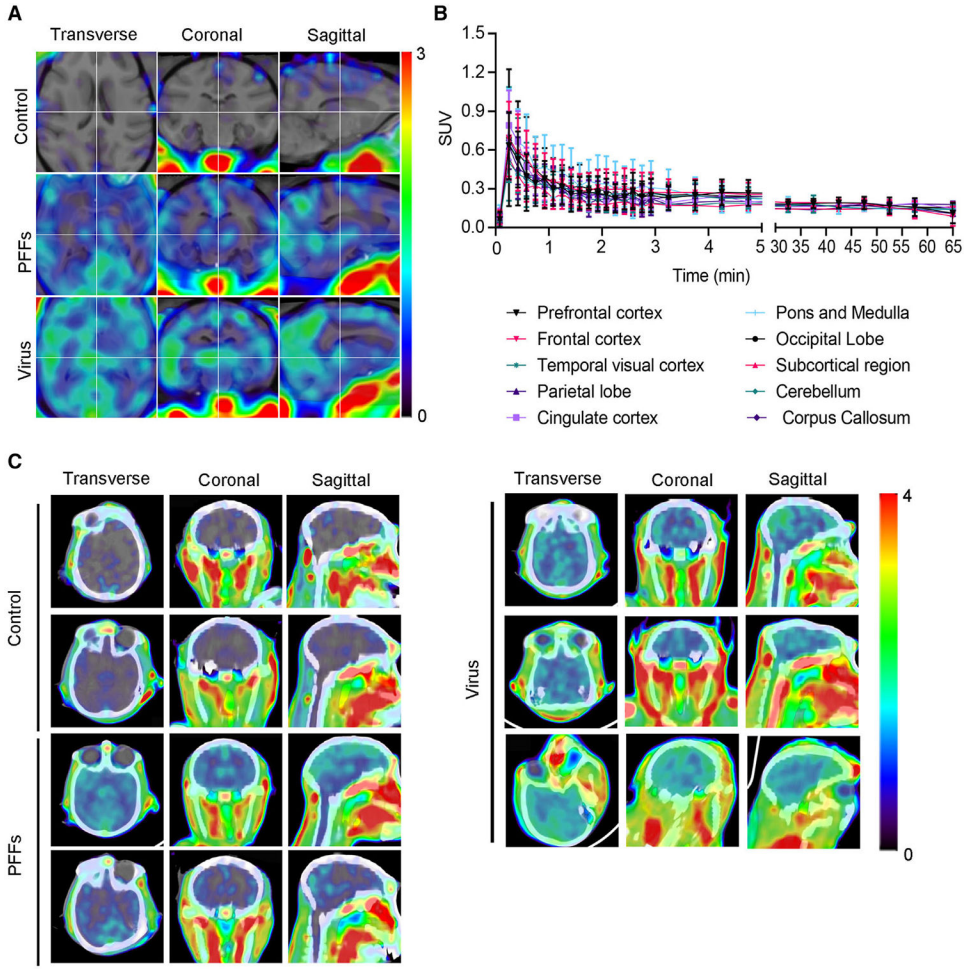

Figure 7. PET imaging of non-human primate PD models with [^{18}F]-F0502B

(A) [^{18}F]-F0502B detects signals in the brains of macaques injected with α-Syn PFFs and AAV-α-Syn A53T, but not in the brains of control macaques. PET images in each row represent the standardized uptake value (percentage of injected dose per cubic centimeter [%ID/cc] × body weight) averaged over a 30 min period at 60 min post injection, co-registered to an MRI imaging template, from left to right showing axial, coronal and sagittal views.

(B) Time course of the standardized uptake value (SUV) in control macaque brain regions after injection of [^{18}F]-F0502B. Each point represents the average of the three subjects. Error bars represent the mean ± SEM. Data are representative of 3 independent experiments.

(C) PET-CT images of α-Syn aggregates in the brains of control, α-Syn PFFs-, and AAV-α-Syn A53T-injected macaques.

See also Figure S7 and Video S1.

KEY RESOURCES TABLE

REAGENT or RESOURCE	SOURCE	IDENTIFIER
Antibodies		
Phospho-Tau (Ser202, Thr205) Antibody (AT8)	Thermo fisher	MN1020, RRID:AB_223647
Anti-α-Syn (phosphor-S129) Antibody	Abcam	ab59264, RRID:AB_2270761
Anti-β-Amyloid, 1-16 Antibody (clone 6E10)	Biolegend	SIG-39300, RRID:AB_662807
Ubiquitin Antibody	Santa Cruz	SC-8017, RRID:AB_628423
Anti-Aggregated α-Synuclein Antibody (clone 5G4)	Millipore	MABN389, RRID:AB_2716647
Anti-rabbit IgG(H+L), F(ab')2 Fragment (Alexa Fluor® 594 Conjugate)	Cell signaling	8889, RRID:AB_2716249
Anti-mouse IgG (H+L), F(ab')2 Fragment (Alexa Fluor® 594 Conjugate)	Cell signaling	8890, RRID:AB_2714182
Bacterial and virus strains		
E. coli BL21 (DE3)	Tiangen Biotech	Cat# CB105
AAV9-A53T-aSyn	Emory Virus Core	N/A
Biological Samples		
Human brain tissue (see detail information in Table S6)	Emory ADRC	N/A
Chemicals, peptides, and recombinant proteins		
Human α-Syn pre-formed fibrils	Homemade	N/A
Beta-amyloid (1-42)	ANA Spec	AS-GMP-20276-1
Human recombinant Tau	Homemade	N/A
rotenone	ULTRA Scientific	Cat# PST-890
ThT	Sigma	S96200
ThS	Sigma	T1892
Critical commertial assays		
Histostain-SP kit	Invitrogen	Cat# 95-9943
Deposited Data		
α-Syn fibril-F0502B complex cryo-EM map	Electron Microscopy Data Bank #EMD-32615	https://www.emdataresource.org/EMD-32615
α-Syn fibril-F0502B complex atomic model	Protein Data Bank #7WMM	https://www.rcsb.org/structure/7WMM
apo-α-Syn fibrils structural models	Protein Data Bank #6A6B	https://www.rcsb.org/structure/6A6B
MSA type I structural models	Protein Data Bank #6XYO	https://www.rcsb.org/structure/6XYO
MSA type II_1 structural models	Protein Data Bank #6XYP	https://www.rcsb.org/structure/6XYP
MSA type II_2 structural models	Protein Data Bank #6XYQ	https://www.rcsb.org/structure/6XYQ
Lewy fold structural models	Protein Data Bank #8A9L	https://www.rcsb.org/structure/8A9L
Experimental models: Organisms/strains		
3XTG mice	The Jackson Laboratory	034830, RRID:MMRRC_034830-JAX
5xFAD mice	The Jackson Laboratory	034840, RRID:MMRRC_034840-JAX
Tau P301S mice	The Jackson Laboratory	008169, RRID:IMSR_JAX:008169
SNCA Tg mice	The Jackson Laboratory	017682, RRID:IMSR_JAX:017682
Software and algorithms		

REAGENT or RESOURCE	SOURCE	IDENTIFIER
Image J 1.53	Schneider et al.[60]	https://imagej.nih.gov/ij/
Graph Pad Prism 8	GraphPad	https://www.graphpad.com/scientific-software/prism
FV31S-DT 2.6	Olympus	https://www.olympus-lifescience.com/
RELION 3.1	Scheres[32]	https://relion.readthedocs.io/en/release-3.1/index.html
COOT	Emsley et al.[61]	https://www2.mrc-lmb.cam.ac.uk/personal/pemsley/coot/
PHENIX	Adams et al.[62]	https://phenix-online.org/
PMOD	Qiu et al.[63]	https://www.pmod.com/web/
syngo.via	Bindoli et al.[64]	https://www.siemens-healthineers.cn/medical-imaging-it/clinical-imaging-applications